

**NATIONAL INSTITUTE FOR FUSION SCIENCE****Study of Toroidal Current Penetration during  
Current Ramp in JIPP T-IIU with  
Fast Response Zeeman Polarimeter**

H. Kuramoto, K. Toi, N. Haraki, K. Sato, J. Xu, A. Ejiri,  
K. Narihara, T. Seki, S. Ohdachi, K. Adati, R. Akiyama,  
Y. Hamada, S. Hirokura, K. Kawahata and M. Kojima

(Received - Jan. 7, 1997 )

NIFS-477

Jan. 1997

**RESEARCH REPORT**  
**NIFS Series**

This report was prepared as a preprint of work performed as a collaboration research of the National Institute for Fusion Science (NIFS) of Japan. This document is intended for information only and for future publication in a journal after some rearrangements of its contents.

Inquiries about copyright and reproduction should be addressed to the Research Information Center, National Institute for Fusion Science, Nagoya 464-01, Japan.

# Study of Toroidal Current Penetration during Current Ramp in JIPP T-IIU with Fast Response Zeeman Polarimeter

H.KURAMOTO<sup>1)</sup>, K.TOI, N.HIRAKI<sup>1)</sup>, K.SATO, J.XU, A.EJIRI,  
K.NARIHARA, T.SEKI, S.OHDACHI, K.ADATI, R.AKIYAMA,  
Y.HAMADA, S.HIROKURA, K.KAWAHATA, M.KOJIMA

National Institute for Fusion Science, Nagoya 464-01, Japan

1) Kyushu Institute of Technology, Iizuka 820, Japan

## Abstract

The toroidal current penetration is studied in current ramp experiments of the JIPP T-IIU tokamak. The poloidal magnetic field profile in the peripheral region of a plasma ( $0.5 \leq \rho \leq 1.0$ ) has been measured directly with a newly developed fast response Zeeman polarimeter. The experimental results indicate that an obvious skin effect of toroidal current density is clearly observed during both the current ramp-up and ramp-down experiments. The experimentally obtained toroidal current density profiles are well described by the profiles calculated on the assumption of the neoclassical electrical conductivity. Quasi-linear  $\Delta'$ -analysis of tearing modes for the measured current density profile is consistent with time behaviour of coherent MHD modes such as  $m=4/n=1$  or  $m=3/n=1$  ( $m$ : poloidal mode number,  $n$ : toroidal mode number) often observed during the current ramp-up phase. The effect of these MHD modes on current penetration during the current ramp-up discharges is studied.

*Key Words: Tokamak Plasma, Toroidal Current Penetration, Zeeman Polarimeter,  
Neoclassical Electrical Conductivity, Tearing Modes*

## 1. INTRODUCTION

In a tokamak plasma, the poloidal magnetic field profile closely depends on the current density profile, which plays an important role in MHD stability and plasma confinement. The current density profile control is important for achieving enhanced tokamak confinement. In JIPP T-II, a stable high-density plasma was obtained with the current density profile control[1]. Recently, it is demonstrated during intense auxiliary heatings that time dependent control of the current density profile is very effective to achieve high- $\beta_t$  and enhanced confinement. The current density profile control is carried out with current ramp experiments where the plasma current is rapidly ramped up or down[2-10]. These experiments have demonstrated that the current density profile control is very effective to obtain enhanced plasma confinement. Moreover, the current ramp-down experiments in JIPP T-IIU have suggested that the L-H transition might be controlled by change of the magnetic shear or magnetic field structure near the plasma edge associated with the radial modification of the edge current density profile[11,12]. It is important to clarify the current penetration in the current profile control experiments.

The current penetration is studied on many tokamaks during the initial current rise phase and rapid current ramp-up in the quasi-stationary phase[13-17]. On JET, time evolution of the toroidal current density profile is well described by neoclassical resistivity at steady state discharge, but the current penetration during the current rise phase is much faster than that expected from the neoclassical resistivity[13]. The current ramp-up experiments have been performed in plasmas with and without sawteeth on TEXT[14]. It is found in this study that there is no need to assume that a large anomalous resistivity exists during rapid current ramp. Neoclassical current diffusion is observed in current ramp-up experiments of Doublet III[15], as far as the ramp-rate is  $dI_p/dt < 7\text{MA/s}$ . As mentioned above, the toroidal current density profile plays an important role in MHD stability and confinement of a tokamak plasma. However, mechanisms of the current penetration are still unclear, because the current density or

poloidal magnetic field profile is not directly measured with enough time and spatial resolutions.

Several methods of internal magnetic field measurement have been proposed and applied to actual experiments. Principal methods are as follows: Faraday rotation measurements[18], measurements of Zeeman splitting of resonance line emission of injected lithium[19], measurements of intensity difference between two circularly polarized visible lights[20,21] and measurements of motional Stark effect(MSE)[22]. We have adopted the method based on refs. 20 and 21, because it is simple and compact and is suitable for the current penetration study. In order to clarify the current penetration in the JIPP T-IIU plasma, we have developed a Zeeman polarimeter with high time resolution[23]. A specially developed Fabry Perot interferometer has allowed us the poloidal field measurement with time resolution up to 1.5ms. High signal-to-noise(S/N) ratio is achieved by using the correlation technique based on Fast Fourier Transform. This polarimeter was successfully employed in the rapid current ramp experiments. The preliminary results are presented in ref.24.

In this paper, we present the results of investigation of current penetration during current ramp experiments on JIPP T-IIU. The time evolution of the poloidal magnetic field and current density profiles are measured using a newly developed Zeeman polarimeter. The effect of the current ramp-rate on the current penetration is also studied on current ramp-up and ramp-down experiments. Moreover, the relation between the current penetration and MHD activities is studied in current ramp-up discharges. The measured profiles are compared with the profiles calculated by the magnetic diffusion equation based on the neoclassical electrical conductivity.

In Section 2, the experimental set-up and details of the Zeeman polarimeter are described. In Section 3, we present the experimental results for current ramp experiments. The current ramp-up experiments are described in Subsection 3.1 and the current ramp-down experiments in Subsection 3.2. In Subsection 3.3, the effects of high and low current ramp rate are described. In Subsection 3.4, the detailed time evolution of

the current density are described. In Subsection 3.5, the effects of MHD activity on current penetration are discussed. In Section 4, we compare the experimental results with those calculated on the assumption of the neoclassical electrical conductivity. In this Section, the stability of the experimentally obtained current density profile against tearing modes is also investigated by using quasi-linear  $\Delta'$ -analysis. Section 5 summarizes the results of these experiments.

## 2. EXPERIMENTAL SET-UP

### 2-1. DEVICE AND DIAGNOSTICS

The JIPP T-IIU device is a medium size tokamak with major radius  $R=0.91\text{m}$  and minor radius  $a=0.23\text{m}$ [25]. In these experiments, the toroidal field is 2.9~3.0T at the plasma center. The electron temperature profile is obtained both by a 28-channel Thomson scattering system and by a 10-channel grating polychromator for electron cyclotron emission (ECE) measurements. The electron density profile is obtained both by the Thomson scattering and by a 6-channel HCN laser interferometer system. The effective charge  $Z_{eff}$  is estimated from visible bremsstrahlung emission. Two sets of poloidal array of magnetic probes are installed inside the vacuum chamber to measure the magnetic fluctuations. The location of the safety factor  $q=1$  surface is inferred from soft-X-ray and ECE signals. The poloidal magnetic field profile in the plasma interior region ( $r/a<0.6$ ) is measured by Motional Stark Effect polarimetry[26] in particular current ramp-up discharges. This Zeeman polarimeter developed for current penetration study is applicable to the peripheral region of  $0.5\leq r/a \leq 1.0$ , because the HeII line is localized there.

### 2-2. ZEEMAN POLARIMETER

The magnetic field measurement is based on the determination of the intensity difference between two circularly polarized profiles of a visible spectral line[20,21]. The

maximum of the difference between left-hand [ $I_L(\lambda)$ ] and right-hand [ $I_R(\lambda)$ ] circularly polarized profiles for the wavelength is given by

$$\max_{\lambda} \left( \frac{I_L - I_R}{I_0} \right) = \sqrt{2} \cos \gamma \frac{\Delta\lambda_B}{\Delta\lambda} = C \times \frac{B \cos \gamma}{\Delta\lambda} \quad (1)$$

where  $C$  is a numerical constant,  $I_0$  is the maximum intensity of the line profile,  $\gamma$  is the angle between the line of sight and the magnetic field line,  $\Delta\lambda$  is the full width at half-maximum (FWHM) of the line, and  $\Delta\lambda_B$  is the Zeeman splitting width. Thus, the difference of circularly polarized profiles is directly proportional to the component of the magnetic field in the line of sight, that is,  $B \cos \gamma$ . If the line of sight is in the poloidal direction of a tokamak device, the poloidal magnetic field can be directly derived from this method.

Figure 1 shows a schematic of the polarimeter installed on the JIPP T-IIU tokamak. As in the figure, this system consists of the photoelastic modulator (PEM), bandpass filter (BF), polarizing beam splitter (PBS), Fabry-Perot (F-P) interferometer and photomultiplier tube as a detector. Also, the carbon tiles are installed inside vacuum chamber to avoid the effects of the reflected light. Fundamental parameters of F-P, PEM, BF and PBS are listed up in Table 1.

A fast scanning of a spectral line profile in the F-P interferometer is performed with three sets of piezoelectric elements and distortion gauges. These piezoelectric elements are driven independently each other by feedback-controlling output signals of distortion gauges, so that this technique enables to control the distance between the etalons with high precision and high stability. The distance between the etalons oscillates in triangle wave form with maximum frequency of 30Hz and maximum peak-to-peak amplitude of about  $2\mu\text{m}$ . When the peak-to-peak amplitude is set at the maximum value of about  $2\mu\text{m}$ , ten or eleven interference patterns may appear in half period. Thus, the maximum scanning time of the line profile is achieved up to 1.5ms.

Both circular polarized lights are distinguished by using PEM and PBS. The PEM converts both circular polarized lights to linear polarized lights orthogonal each other. That is, one of linear polarization axis is at  $+45^\circ$  with respect to the optical axis of PEM and other is at  $-45^\circ$ . Thus, using the PBS we can split two circular polarized lights into orthogonal linearly polarized lights. Also, the PEM acts as a quarter-wave plate oscillating in 50kHz, so that the retardation produced by PEM is switched from  $-\lambda/4$  to  $+\lambda/4$ .

Two output signals from this system are expressed as

$$I_{\pm} = \frac{1}{2}(I_L + I_R) \pm (I_L - I_R) \sin \omega_m t \quad (2)$$

where  $t$  is time,  $\omega_m$  is the modulation angular frequency of retardation in PEM. Each signal is detected by each photomultiplier tube. The outputs  $I_+$  and  $I_-$  are analyzed by a correlation procedure based on Fast Fourier Transform (FFT), instead of a lock-in amplifier which was usually used in measurements of low S/N ratio signals. This procedure is shown in Fig.2. The line profile signal  $(I_L+I_R)$  is detected by adding output signals  $I_+$  and  $I_-$  and using the FFT-based lowpass filter. The signal  $(I_L-I_R)\sin\omega_m t$  is detected by subtracting output signals, and pick up a component of  $40 < f < 60$ kHz using the FFT-based bandpass filter, where  $\omega_m/2\pi=50$ kHz. To remove noise induced by plasma fluctuations around  $\omega_m/2\pi$  from the output of the bandpass filter, only component highly correlated with the reference signal from PEM in the output is derived by the time averaging over one cycle of the modulation, i.e.,  $T=2\pi/\omega_m$ . The modulation signal  $(I_L-I_R)$  is successfully derived by this procedure from signals contaminated by various types of noise such as hard X-ray and electromagnetic waves.

Figure 3 shows an example of  $(I_L-I_R)$  and  $(I_L+I_R)$  signals obtained in the current ramp-up discharges of JIPP T-IIU. Figure 3(A) shows time evolution of the plasma current and the sum signal  $(I_L+I_R)$  and the difference signal  $(I_L-I_R)$  obtained from the procedure shown in Fig.2. As seen from Figs 3(B) and (C), signals  $(I_L+I_R)$  and  $(I_L-I_R)$  clearly show the specific shapes, that is, the Doppler broadened spectral line profile and

polarization modulation, respectively. The signal  $(I_L+I_R)$  is well described by the Gaussian profile, and the signal  $(I_L-I_R)$  by the deference between two shifted Gaussian profiles. The maximum intensity of the line profile,  $I_0$ , and the FWHM of the line,  $\Delta\lambda$ , are determined from the fitting of line profile signal  $(I_L+I_R)$ . The maximum deference between left-hand and right-hand circularly polarized profiles for the wavelength,  $\max(I_L-I_R)$ , is determined from the modulation signal shape in time, where the time corresponds to the wavelength in the free spectral range of the F-P interferometer.

As seen from Eq. (1), the magnetic field strength along the line of sight is proportional to the maximum of the difference between left-hand and right-hand circularly polarized profiles and the FWHM of the line, and is inversely proportional to the maximum intensity of the line profile. However, the numerical coefficient  $C$  depends on the fine structure of the spectral line. The numerical coefficient  $C$  in Eq. (1) is determined from the measurement of the known toroidal field by using this polarimeter of which line of sight is adjusted to pass though the magnetic axis. The component of the toroidal field,  $B_T \sin \alpha$ , is observed in the toroidal direction with the angle  $\alpha$  of  $\pm 3.5^\circ$ , where  $\alpha$  is the angle between the line of sight on the equatorial and the toroidal field. The calibration experiment is performed by changing the strength of toroidal field,  $B_T=2.1\text{T}, 2.7\text{T}, 3.0\text{T}$ . The results are summarized in Fig.4, and then the numerical coefficient is estimated as  $C=0.340\pm 0.003$  ( $\text{\AA}/\text{T}$ ) which agrees well with the theoretical value assuming  $z=1.17$  for the HeII 4686 $\text{\AA}$  case.

The poloidal magnetic field measurement at the plasma edge is also performed to calibrate the polarimeter signal, because the poloidal field at the plasma edge is accurately estimated from the total plasma current. The poloidal fields obtained from the polarimeter signal using the above numerical coefficient  $C$  are shown by open circle in Fig.5. The solid line is estimated from the total plasma current, as  $B_\theta(a)=\mu_0 I_{tot}/(2\pi a)$ . The error bar is estimated to be about 3% typically, from the accuracy of the calibration of  $C$  and the fitting of the following parameter  $I_0$ ,  $\Delta\lambda$ , and  $(I_L-I_R)$  shown in Fig.3. It is found that the poloidal magnetic field measured by the Zeeman polarimeter agrees well



with that calculated from the total plasma current. It is clearly demonstrated that this newly developed Zeeman polarimeter can be effectively employed to measure the poloidal field strength in a Tokamak plasma.

In this system, the HeII 4686Å line is adopted as a monitoring spectral line. Throughout these experiments, helium gas is doped up to 30% in deuterium plasma. The line intensity must be localized near the plasma edge region of a high temperature plasma. This is usually disadvantageous for plasma diagnostics because of limited observation area. However, it is advantageous to study the current penetration in the plasma peripheral region. In the present experiments, this polarimeter was applicable in the region of  $0.5 \leq \rho \leq 1$  with high S/N ratio because of sufficient intensity. It should be noted that each Zeeman component of the line contains two strong transitions that are close to each other within  $\sim 0.1 \text{Å}$  wavelength difference. Total transition probabilities of the three Zeeman components are equal because of the sum rule[27], that is, the intensity of each Zeeman component is equal to the sum of the intensity of each transition.

In this method, the measured poloidal field is intrinsically averaged along the line of sight, and an Abel inversion procedure is required to obtain the local values of the poloidal field. If the cylindrical plasma is assumed, the local value is derived from the magnetic field  $B^{mea}$  and the intensity  $I^{mea}$  measured at various measurement positions  $z$ , as follows[20]:

$$B^{real}(r) = -\frac{r}{\pi \varepsilon(r)} \int_r^a \frac{d}{dz} \left( \frac{B^{mea}(z) I^{mea}(z)}{z} \right) \frac{dz}{\sqrt{z^2 - r^2}} \quad (3)$$

where  $\varepsilon(r)$  is the local volume emission coefficient. The inversion procedure introduces only a small correction of 5% to 10% to the measured poloidal field.

### 3. EXPERIMENTAL RESULTS

#### 3-1. CURRENT RAMP-UP EXPERIMENTS

The current ramp-up (CRU) experiments are performed in the JIPP T-IIU tokamak by rapidly increasing the plasma current at about 230ms after the plasma current reaches the first flat-top. A typical CRU discharge is shown in Fig.6. Figure 6 shows time evolution of plasma current  $I_p$ , line-average electron density  $\bar{n}_e$  and electron temperature  $T_e$  from electron cyclotron emission (ECE) measurements. In this discharge, a fuel gas is deuterium and then He gas is added to enhance HeII line intensity. As shown in this figure, the plasma current is ramped-up with  $dI_p/dt \approx 8\text{MA/s}$  from 230ms. The sawtooth oscillations appear from the beginning of the second flat-top, i.e. from  $t \approx 250\text{ms}$ . In this discharge, the poloidal magnetic field profile and toroidal current density profiles are measured by the polarimeter (Fig.7). Because of a single channel of the polarimeter, the poloidal magnetic field profile is obtained on shot-to-shot basis. In Fig.7, open circles show the poloidal field profile before current ramp-up (at 210ms in Fig.6), diamonds show during current ramping (at 240ms), squares show after current ramp-up (at 280ms). The profile of the toroidal current density is derived from the poloidal field profile fitted by a polynomial as shown in the upper figure of Fig.7. The error bars are estimated from fitting procedure when obtained the three values shown in Fig.3 and Abel inversion procedure, which have a maximum value of about  $\pm 10\%$  at the half of the plasma radius. It is seen from Fig.7 that the poloidal magnetic field and the toroidal current density penetrate gradually from plasma edge to interior. It is also found that the current density profile near the plasma edge exhibits a clear skin effect. The skin effect almost disappears about 50ms later from the turn-on of the ramp-up.

#### 3-2. CURRENT RAMP-DOWN EXPERIMENTS

The current ramp-down (CRD) experiments are also performed in the JIPP T-IIU tokamak by rapidly decreasing the plasma current. A typical CRD discharge is shown in

Fig.8. In this shot, the plasma current is rapidly ramped-down with  $dI_p/dt \approx -8\text{MA/s}$  from 230ms. The electron temperature at the plasma center gradually decreases during the current ramp-down. In this discharge, a fuel gas is deuterium and He gas is added to enhance HeII line intensity, as is similar to the CRU experiments. The sawtooth activities are observed on the ECE signals before and during the current ramp-down. It is found from ECE data that the size of  $q=1$  surface is larger than  $\sim 6\text{cm}$  before CRD and is obviously decreased just before the end of the ramp-down. In the upper figure of Fig.9, open circles show the poloidal magnetic field profile before current ramp-down (at 210ms in Fig.8), diamonds show during current ramping (at 240ms), squares show after current ramp-down (at 280ms). The magnetic field and current density profiles also penetrate to interior region from plasma edge, and indicate the inversed skin effect in the region  $\rho \approx 0.75-1.0$ . This means that the current in this region flows in the reversed direction against the plasma interior.

### 3-3. EFFECT OF CURRENT RAMP RATE ON CURRENT PENETRATION

We have studied the dependence of the current ramp rate ( $dI_p/dt$ ) on the current penetration. The experiments have been performed for the plasma current ramp rate about  $\pm 4\text{MA/s}$  and  $\pm 8\text{MA/s}$  (Fig.10), where the toroidal field and line averaged electron density are  $3.0\text{T}$  and  $4\sim 5 \times 10^{19}\text{m}^{-3}$  for both cases. As shown in the figure, the initial plasma current is same and the plasma current is ramped-up or ramped-down to the second flat-top. The current density profiles measured in this experiment are shown in Figure 11. The bold curves indicate the current density profiles in the discharges with the higher ramp rate and the thin curves profiles in the discharges with the lower one, respectively. Also, the solid, broken and dotted curves correspond to the profiles before the current ramp (at  $t=210\text{ms}$ ), during the current ramping (at the time indicated by arrows in Fig.10) and after the current ramp (at  $t=280\text{ms}$ ), respectively. In this figure, it is found that the current density profiles during CRD are similar in both cases, that is, low and

high current ramping rate. On the other hand, the current density profiles during CRU show an obvious difference. However, these measured profiles for both CRU and CRD discharges agree well with the calculated profiles on the assumption of neoclassical electrical conductivity. The reason why the small difference in the current density profiles during CRD is thought to be the appreciable decrease in electron temperature near the edge in the faster ramp-down rate.

### 3-4. DETAILED TIME EVOLUTION OF CURRENT DENSITY PROFILE

In this subsection, we discuss the current penetration process more in detail.

Figure 12 shows time evolution of the current density at each radial position in four cases discussed in subsection 3-3. Figure 12(A) shows the case with the lower current ramp-up rate (about 4MA/s) and (B) shows the case with the higher current ramp-up rate (about 8MA/s). In both cases the current density near the edge is rapidly increased, exhibiting the obvious skin effect. The skin profile gradually propagates toward the plasma interior, losing the skin effect. Figure 12(C) shows the case with the lower current ramp-down rate (about -4MA/s) and (D) shows with the higher current ramp-down rate (about -8MA/s). Both cases show the obvious skin effect, and the current density near the edge is rapidly decreased through the reversed skin effect induced by the rapid current ramp-down. The current penetration is similar on these CRU and CRD plasmas.

Assuming the radial profile of electric conductivity  $\sigma(r)$  is uniform for simplicity, time evolution of the current density profiles is calculated from the magnetic diffusion equation in a cylindrical plasma as follows:

$$j_{\varphi}(r,t) = \frac{A a j_0}{2\sqrt{\pi a r t}} \exp\left[-\frac{A^2(a-r)^2}{4t}\right] \quad (4)$$

where  $A$  is the square root of the product of the vacuum magnetic permeability and the electric conductivity, i.e.  $A^2 = \mu_0 \sigma$ . This equation suggests that the arrival time of the

peak current density at each position is proportional to the square of the distance from the plasma edge if the current penetration is governed only by a diffusive process. Figure 13 shows the arrival time of the peak of current density  $j_{\varphi}(r,t)$  for four cases shown in the Fig.12. In this figure, open circles indicate the arrival time obtained from the experimental data. Solid curves indicate the arrival time calculated by the magnetic diffusion equation, which will be discussed in the following section. As seen from Fig.12, the calculated results agree well with the experimental ones.

### **3-5. EFFECT OF MHD ACTIVITIES ON CURRENT PENETRATION**

It was reported from ASDEX[16] and PDX[17] that anomalous current penetration was induced by MHD activities excited during the current ramp-up. To compare our results to above reports, we have carefully studied the current penetration in the current ramp-up discharge with coherent MHD activities. This type of discharge is obtained in the current ramp-up with higher ramp rate of  $\sim 8\text{MA/s}$  ( Fig.10 ). Figure 14 shows time evolution of plasma current and safety factor at the plasma surface, current density measured by the Zeeman polarimeter at each position, and magnetic probe signal. As shown in this figure, MHD oscillations appear at 238ms. It is concluded that any enhanced current penetration caused by coherent MHD modes is not found in the discharge discussed in Fig.14.

## **4. COMPARISON WITH NEOCLASSICAL CURRENT PENETRATION**

### **4-1. MAGNETIC DIFFUSION EQUATION**

The toroidal current density and the poloidal magnetic field profiles may be derived indirectly by using experimentally obtained electron temperature and density profiles. When the electrical conductivity profile is known, the safety factor  $q(r)$  profile is calculated by solving the following magnetic diffusion equation for the cylindrical geometry,

$$r \frac{\partial}{\partial t} \left[ \frac{1}{q(r,t)} \right] = \frac{1}{\mu_0} \frac{\partial}{\partial r} \left[ \frac{1}{r\sigma(r,t)} \frac{\partial}{\partial r} \left( \frac{r^2}{q(r,t)} \right) \right] \quad (5)$$

where  $q(r)=rB_T/(RB_\theta(r))$ . The current density profile is straight formally obtained from the above results, using Maxwell's equation. In this analysis, we assume the following neoclassical electrical conductivity[28],

$$\sigma = \sigma_0 T_e^{3/2} \left[ 1 - \frac{1.9\sqrt{r/R} - r/R}{1 + \nu_e^*} \right] \frac{1}{\gamma(Z_{eff})} \quad (6)$$

where

$$\nu_e^* = \frac{(1 + Z_{eff})R^{3/2}B_T}{2\tau_e r^{1/2} B_\theta (k_B T_e / m_e)^{1/2}} \quad (7)$$

and

$$\gamma(Z_{eff}) = Z_{eff} \left( 0.29 + \frac{0.457}{1.077 + Z_{eff}} \right) \quad (8)$$

where  $m_e$ ,  $k_B$  and  $Z_{eff}$  are the electron mass, Boltzmann constant and effective charge of a plasma, respectively. The analysis is carried out by adjusting the  $Z_{eff}$  profile so that the calculated loop voltage and the location of  $q=1$  surface are fit for the experimental data[1]. Moreover, the calculated average  $Z_{eff}$  values are also compared to the experimental values derived from visible bremsstrahlung measurements.

#### 4-2. COMPARISON BETWEEN THE MEASURED AND CALCULATED PROFILES

We have tested effectiveness of the above method in a typical CRU discharge. In this discharge, the poloidal magnetic field profile is measured over a whole plasma radius by using both Zeeman polarimeter focusing on the peripheral region ( $0.5 \leq \rho \leq 1.0$ ) and Motional Stark Effect (MSE) Polarimetry on the interior region ( $0 \leq \rho \leq 0.5$ ). Figure 15 shows the comparison between experimentally obtained  $Z_{eff}$  value, loop voltage and the location of the  $q(r)=1$  with those calculated by the above mentioned procedure, where the

$Z_{eff}$  value derived from visible bremsstrahlung is adjusted to fit for the calculated value at  $t=200$ ms, because it is uncalibrated. The open circles denote the calculated values and agree well with the measured values shown by solid curves and circles. The locations of the  $q=1$  surface obtained by ECE signals contain uncertainty of about  $\pm 1.2$ cm. The dramatic change of the average  $Z_{eff}$  takes place just after pellet injection (at  $t \approx 250$ ms). As seen from Fig.15, the calculated values agree well with the measured values. In Fig.16, these calculated poloidal field profiles are compared to the profiles measured by the Zeeman Polarimeter and MSE polarimetry, where curves and points correspond to calculated and measured profiles. The circles and solid line indicate the poloidal magnetic profiles just before CRU (at 190ms), where CRU is started at 203ms (Fig.15) and finished at  $\sim 230$ ms. The squares and large broken line indicate the profiles at 210ms, and the diamonds and middle broken line indicate the profiles at 230ms, both of which are during CRU. The triangles and small broken line indicate the profiles at 250ms and inverted triangles and dotted line indicate the profiles at 270ms, which are after CRU. It is found that the poloidal field profiles calculated on the assumption of the neoclassical electrical conductivity are in good agreement with the measured profiles by both Zeeman polarimeter and Motional Stark Polarimetry.

It is important to know what collisionality regime the above discussed discharge belongs to. Figure 17 shows time evolution of the neoclassical correction factor in the electrical conductivity,

$$f_{Tr} = 1 - \frac{1.9\sqrt{r/R} - r/R}{1 + \nu_e^*}, \quad (9)$$

and effective collisionality in the discharge shown in Fig.16. The area of  $\nu_e^* < 1$  corresponds to the banana regime, that of  $1 < \nu_e^* < (r/a)^{3/2}$  to the plateau regime, and that of  $\nu_e^* > (r/a)^{3/2}$  to the collisional or MHD regime. The shaded area indicates the area which is not measured by using Zeeman polarimeter. The collisionality just before CRU (at 200ms) is large enough near the plasma edge, so that  $f_{Tr}$  is approximately equal 1. The

collisionality here decreased during CRU, because  $B_\theta$  is increased near the edge. This region goes into the plateau regime. After CRU, the collisionality again increases and  $f_{Tr}$  approaches 1. In the interior region of  $5 \leq r \leq 12 \text{cm}$ , the collisionality is hardly changed and to be  $f_{Tr} \approx 0.75-0.8$ .

In Fig.18 the measured and calculated current density profiles are compared for the CRU and CRD discharges, where the lines show the calculated profiles by solving the magnetic diffusion equation and the symbols show the profiles measured by the Zeeman polarimeter. The circles and solid lines indicate the poloidal magnetic profiles just before CRU or CRD (at 220ms), where the current ramp is started from 233ms. The squares and large broken lines indicate the profiles at 240ms which corresponds to during CRU or CRD. The diamonds and middle broken lines indicate the profiles at 260ms, and the triangles and small broken lines indicate the profiles at 280ms where both times correspond to after CRU or CRD. As seen from Fig.18, the calculated current density profiles are in good agreement with the measured profiles. It is concluded that penetration of the toroidal current density on current ramp experiments can be described well by the analysis based on the neoclassical electrical conductivity, without introducing any anomalously reduced conductivity ( or anomalous resistivity ).

We have also discussed about time evolution of current density profiles,  $j_\phi(r,t)$ , by using the magnetic diffusion equation. As described in Section 3-4, the arrival time of the peak of current density  $j_\phi(r,t)$  at each position is predicted to be proportional to the square of distance from plasma edge,  $(\Delta r)^2$ , according to the magnetic diffusion in a uniform plasma. However, as shown in Fig.13 the arrival time is not necessarily proportional to  $(\Delta r)^2$ . As seen from Eq.(4), the delay time is proportional to  $(\Delta r)^2$  if  $\Delta r$  is small enough. If  $\Delta r$  become large due to current penetration, the delay time is no longer proportional to  $(\Delta r)^2$ . The non-uniformity of electrical conductivity should be taken account. The fact that the current is not increased as a step function also introduces the deviation of the above relation between the delay time and  $(\Delta r)^2$ . It is necessary to investigate whether or not the non-diffusive nature can be recognized on the current



penetration. The solid curves in Fig.13 are obtained from the magnetic diffusion equation on the assumption of neoclassical conductivity. The calculated results agree very well with the experimental data, and there is no obvious signature of non-diffusive nature in the current penetration.

#### 4-3. MHD STABILITY FOR CURRENT DENSITY PROFILE OBTAINED DURING THE CURRENT RAMP-UP

As discussed above, the obvious skin effect during current ramp is observed. It is interesting to investigate the stability of these current density profiles against kink and tearing modes. In particular, distinct coherent modes such as  $m=4/n=1$  and/or  $3/1$  are observed during the current ramp-up. We have investigated the stability of the measured current density profiles against tearing and kink modes by using quasi-linear  $\Delta'$ -analysis[29]. In this analysis, we have adopted the simplified quasi-linear  $\Delta'$ -analysis, that is, the saturated island size is determined by  $a\Delta'(w=w_s)=0$ , as applied to the previous experiments[30]. The relative amplitude of the poloidal field fluctuations with  $m/n$  mode number is estimated at the plasma surface as follows:

$$\left[ \frac{\tilde{B}_\theta}{B_\theta} \right]_{r=a} = -\frac{q(a)}{16} \left( \frac{n}{m} \right)^2 \left( \frac{w_s}{a} \right)^2 \frac{r_s}{a} \frac{a}{\Psi(r_s)} \left( \frac{d\Psi}{dr} \right)_{r=a} \quad (10)$$

where  $\Psi$  is a perturbed poloidal magnetic flux and  $r_s$  is the radius of the rational surface  $q=m/n$ . For this discharge, the  $m/n=2/1$  mode is unstable until the start of the second flat top of the plasma current. However, the saturated island size is not large and the magnetic fluctuation amplitude is estimated to be fairly low. Also, the calculated fluctuation amplitudes of  $m/n=4/1$  and  $3/1$  mode are strongly enhanced during the current ramp-up, of which fact agrees well with experimental observations. The  $m/n=5/1$  and  $6/1$  modes are stable during the current ramp-up. Analyzed results are shown in Fig.19. As seen from Fig.19, time behaviors of calculated  $(\tilde{B}_\theta / B_\theta)_{r=a}$  agree well with the time evolution of  $m/n=4/1$  mode with the frequency  $f=5\sim 12\text{kHz}$  and  $m/n=3/1$  mode with  $f=2\sim 6\text{kHz}$ , detected by magnetic probes.

## 5. CONCLUSIONS

We have developed a Zeeman polarimeter which derives the magnetic field strength along the line of sight from measurements of the difference of left-hand and right-hand circularly polarized visible spectral lines, which is HeII 4686Å. This polarimeter having up to 1.5ms time response is successfully applied to current penetration studies in helium doped plasmas of the JIPP T-IIU tokamak, where the central electron temperature and density are in the range of  $T_e(0) \leq 1.5\text{keV}$  and  $n_e(0) \leq 1 \times 10^{20}\text{m}^{-3}$ . In these experiments, helium gas is doped to enhance the HeII intensity in the peripheral region which is the most relevant area for the toroidal current penetration. This introduces disadvantage that the measurement is restricted only in the cold edge region, but the measurements have been successfully performed in the region of  $r/a \geq 0.5$  on JIPP T-IIU. If HeII line emitted through charge exchange recombination with injected neutral beams is employed, the above limitation may be reduced.

Time evolution of the toroidal current is measured with this fast-response Zeeman polarimeter in rapid current ramp-up and ramp-down discharges ohmically or NBI heated. During the current ramp-up and ramp-down up to  $\pm 8\text{MA/s}$  ramp-rate a clear skin effect in the toroidal current density profile is observed and decays due to the current penetration. It is confirmed for the first time by direct measurements of poloidal magnetic field that the time evolution of the toroidal current density profiles is well described by magnetic diffusion calculation based on neoclassical electrical conductivity, although most of studies are carried out in the plateau and collisional regimes of the neoclassical transport theory. It is also found that the current penetration is not obviously affected by the presence of low  $m$  tearing modes excited near the edge during current ramp-up. This suggests that neoclassical electrical conductivity along the magnetic field line is applicable to analyze the current penetration in the tokamak plasma, at least in plateau and collisional regimes. The skin current profile observed during rapid current ramp-up is confirmed to be unstable against  $m=4/n=1$  and/or  $3/1$  by a quasi-linear  $\Delta'$ -analysis, of which results are consistent with magnetic fluctuations detected with magnetic probes.

## Acknowledgments

Authors gratefully acknowledge useful discussions with the rest of members of the torus experiment group in National Institute for Fusion Science.

## REFERENCES

- [1] TOI, K., ITOH, S., KADOTA, K., KAWAHATA, K., NODA, N., et al., Nucl. Fusion 19(1979) 1643.
- [2] BELL, M.G., McGUIRE, K.M., ARUNASALAM, V., BARNES, C.W., BATHA, S.H., et al., Nucl.Fusion 35 (1995) 1429.
- [3] ZARNSTORFF, BARNES, C.W., EFTHIMION, P.C., HAMMETT, G.W., HORTON, W., et al., in Plasma Physics and Controlled Nuclear Fusion Research 1990(Proc. 13th Int. Conf. Washington, DC, 1990), Vol.1, IAEA, Vienna(1991) 109.
- [4] SABBAGH, S.A., GROSS, R.A., MAUEL, M.E., NAVRATIL, G.A., BELL, M.G., et al., Phys. Fluids B3 (1991) 2277.
- [5] LEVINTON, F.M., ZARNSTORFF, M.C., BATHA, S.H., BELL, M., BELL, R.E., et al., Phys. Rev Lett. 75 (1995) 4417.
- [6] CHALLIS, C.D., CHRISTIANSEN, J.P., CORDEY, J.G., GORMEZANO, C., GOWERS, C.W., et al., Nucl. Fusion 32 (1992) 2217.
- [7] KIMURA, H., the JT-60 TEAM, Phys.Plasmas 3(1996) 1951.
- [8] LAO, L.L., FERRON, J.R., TAYLOR, T.S., CHAN, V.S., OSBORNE, T.H., et al., in Plasma Physics and Controlled Nuclear Fusion Research 1992(Proc. 14th Int. Conf. Würzburg, 1992), Vol.1, IAEA, Vienna(1993) 565.
- [9] FERRON, J.R., LAO, L.L., TAYLOR, T.S., KIM, Y.B., STRAIT, E.J., et al., Phys. Fluids B5(1993) 2532.
- [10] MURMANN, H., et al., in Controlled Fusion and Plasma Physics (Proc. 18th Eur. Conf. Berlin, 1991), Vol. 15C, Part I, European Physical Society (1991) 109.
- [11] TOI, K., KAWAHATA, K., MORITA, S., WATARI, T., KUMAZAWA, R., et al., Phys. Rev. Lett.64, (1990)1895.
- [12] TOI, K., MORITA, S., KAWAHATA, K., IDA, K., WATARI, T., et al., in Plasma Physics and Controlled Nuclear Fusion Research 1992(Proc. 14th Int. Conf. Würzburg, 1992), Vol.1, IAEA, Vienna(1993) 519.
- [13] CAMPBELL, D. J., LAZZARD, E., NAVE, M.F.F., CHRISTIANSEN, J.P., CORDEY, J.G., et al., Nucl. Fusion 28(1988) 981.
- [14] PORTER, J.L., PHILLIPS, P.E., McCOOL, S.C., KIM, S.B., ROSS, D.W., et al., Nucl. Fusion 27(1987) 205.

- [15] STAMBAUGH, R.D., BLAU, F.P., EJIMA, S., JAHNS, G.L., LUXON, J.L., et al., Nucl. Fusion 22 (1982) 395.
- [16] KARGER, K., KLUBER, K., NIEDERMEYER, H., SCHULLER, F.C., THOMAS, P.R., et al., in Controlled Fusion and Plasma Physics (Proc. 11th Eur. Conf. Aachen, 1983), Vol. 7D, Part I, European Physical Society (1983) 63.
- [17] MEYERHOFER, D.D., GOLDSTON, R.J., KAITA, R., CAVALLO, A., GREK, B., et al., Nucl. Fusion 25 (1985) 321.
- [18] SOLTWISH, H., Rev.Sci.Instrum. 57(1986) 1939.
- [19] WEST, W.P., THOMAS, D.M., ENSBERG, E.S., DEGRASSIE, J.S., BAUR, J.F., Rev.Sci.Instrum.57 (1986) 1552.
- [20] WROBLEWSKI, D., HUANG, L.K., MOOS, H.W., Rev. Sci. Instrum. 59 (1988) 2341.
- [21] FELDMAN, U., SEELY, J.F., SHEELEY, N.R., et al., J.Appl.Phys.56, 2512(1984).
- [22] WROBLEWSKI, D., LAO, L.L., Rev.Sci.Instrum. 63 (1992)5140.
- [23] KURAMOTO, H., HIRAKI, N., MORIYAMA, S., TOI, K., SATO, K., et al., J.Plasma Fusion Res.71(1995)1020 [in Japanese].
- [24] KURAMOTO, H., HIRAKI, N., MORIYAMA, S., TOI, K., SATO, K., et al., Proceedings of 7th International Toki Conference on Plasma Physics and Controlled Fusion In Press(1995).
- [25] TOI, K., HAMADA, Y., KAWAHATA, K., WATARI, T., ANDO, A., et al., in Plasma Physics and Controlled Nuclear Fusion Research 1990(Proc.13th Int. Conf. Washington D.C.,1990)Vol.1, IAEA, Vienna(1991) 301.
- [26] XU, J., TOI, K., KURAMOTO, H., NISHIZAWA, A., FUJITA, J., et al., National Institute for Fusion Science Report NIFS-397(1996).
- [27] COWAN, R.D., *The Theory of Atomic Structure and Spectra* (University of California Press, Berkeley, CA, 1981).
- [28] DUCHS, D.F., POST, D.E., RUTHERFORD, P.H., Nucl. Fusion 17 (1977) 565.
- [29] WHITE, R.B., MONTICELLO, D.A., ROSENBLUTH, M.N., WADDELL, B.V., Phys. Fluids 20 (1977) 800.
- [30] TOI, K., SAKURAI, K., TANAHASHI, S., YASUE, S., Nucl. Fusion 22 (1982) 465.

## Figure captions

- Fig.1 Experimental setup of the Zeeman Polarimeter on JIPP T-IIU. (A) Schematic view of the optical system on JIPP T-IIU. (B) Detailed arrangement of the Zeeman polarimeter. PEM: photoelastic polarimeter, BF: band-pass filter, PBS: polarizing beam splitter, F-P: Fabry-Perot interferometer.
- Fig.2 Analysis procedure of the polarimeter signals.
- Fig.3 Signals obtained by the analysis procedure shown in Fig.2. (A) Time evolution of a plasma current, the line profile ( $I_L+I_R$ ) and the modulation ( $I_L-I_R$ ) of the spectral line. (B) The enlarged line profile signal and (C) the enlarged signal of the polarization modulation. The solid curves denote profiles fitted with Gaussian profiles.
- Fig.4 Results of the calibration experiment carried out by measuring the toroidal magnetic field, where the line of sight of the polarimeter is tilted around the perpendicular direction in the equatorial plane of the plasma. The amplitude of the toroidal field is also changed 2.1T, 2.7T and 3.0T.
- Fig.5 Time evolution of the poloidal magnetic field at plasma edge. Open circles is the measured poloidal field from Zeeman polarimeter. Solid curve is the poloidal field derived from total plasma current. This indicates the very accurate calibration of the measured magnetic field.
- Fig.6 Time evolution of plasma parameters on the current ramp-up discharge, where  $I_p$ : plasma current,  $\bar{n}_e$ : line-average electron density,  $T_e$ : electron temperature from electron cyclotron emission signal. The arrows in the upper figure show the times when the measured profile shown in Fig.7 are obtained.
- Fig.7 Time evolution of poloidal magnetic field and toroidal current density profile on the current ramp-up discharge. In the upper figure, symbols denote the measured magnetic field, and curves are the profile fitted by a polynomial. Open circles and solid, diamonds and broken curves, and squares and dot-dash curves are obtained at 210ms, 240ms, 280ms in Fig.6, respectively. Current density profiles in a lower figure are derived from the fitted curves shown in the upper figure.
- Fig.8 Time evolution of plasma parameters on the current ramp-down discharge, where  $I_p$ : plasma current,  $\bar{n}_e$ : line-average electron density,  $T_e$ : electron temperature from electron cyclotron emission signal. The arrows in the upper figure show the times when the measured profile shown in Fig.9 are obtained.
- Fig.9 Time evolution of poloidal magnetic field and toroidal current density profile on the current ramp-down discharge. In the upper figure, symbols denote the measured magnetic field and curves are the profile fitted by a polynomial. Open circles and solid, diamonds and broken curves, and squares and dot-dash curves are obtained at 210ms, 240ms, 280ms in Fig.8, respectively. Current density profiles in a lower figure are derived from the fitted curves shown in the upper figure.

Fig.10 Time evolution of the plasma current  $I_p$  in the discharges with different ramp rate. The bold curves indicate the higher ramp rate and the thin curves the lower ramp rate. The values indicate the current ramp rate estimated at  $I_p = 180\text{kA}$ .

Fig.11 Comparison of current density profiles at the various timings in the discharges shown in Fig.10.

The bold curves indicate the higher current ramp rate ( $dI_p/dt \approx 8\text{MA/s}$ ) and the thin curves indicate the lower current ramp rate ( $dI_p/dt \approx 4\text{MA/s}$ ). The solid curves are obtained at before current ramp(i.e., 220ms), the broken curves at during current ramping(i.e., at the times show by arrows in Fig.10) and the dotted curves at after current ramp(i.e., 270ms).

Fig.12 Detailed time evolution of current density at each radial position.

(A) The case is the CRU discharge with the lower current ramp rate (about 4MA/s). (B) The case is the CRU discharge with the higher current ramp rate (about 8MA/s). (C) The case is the CRD discharge with the lower current ramp rate (about -4MA/s). (D) The case is the CRD discharge with the higher current ramp rate (about -8MA/s). The broken lines indicate the each zero level of the current density. Numbers indicate each radial positions of the plasma where the minor plasma radius is 23cm.

Fig.13 The arrival time of the peak of current density  $j_{\phi}(r,t)$  as a function of the squares of the distance from the plasma surface( $\Delta r = a-r$ ).

The open circles indicate the arrival time from the measured current density profile shown in Fig.12. The bold curves indicate the arrival time calculated from the magnetic diffusion equation on the assumption of neoclassical electrical conductivity.

Fig.14 Time evolution of the current ramp-up discharge having MHD activities.

Time evolution of plasma current  $I_p$  and safety factor at plasma surface, current density at each radial position  $j_{\phi}(r,t)$  and magnetic probe signal are shown. The ramp-up rate of this discharge is 8MA/s. In this discharge, strong  $m/n=3/1$  oscillations are excited for 238~241ms.

Fig.15 Comparison of calculated  $Z_{eff}$  value, loop voltage and the size of the  $q(r)=1$  surface with those experimental values, where open circles and curves indicate the calculated and experimental values, respectively.

The experimental line averaged  $Z_{eff}(r)$  is estimated from the visible bremsstrahlung emission. The size of  $q=1$  surface is deduced from the ECE measurements.

Fig.16 Comparison of calculated and measured poloidal magnetic field profiles, where open symbols, closed symbols and the curves are the measured profile from Zeeman polarimeter(ZP), the measured profile from motional stark effect(MSE) Polarimetry and the calculated profile by solving the magnetic diffusion equation, respectively.

The circles and solid curve indicate the poloidal magnetic profiles at 190ms, just before the current ramp-up started from 203ms. The squares and large broken curve indicate the profiles at 210ms and the diamonds and middle broken curve indicate the profiles at 230ms, which are during the current ramp-up. The triangles and small broken curve indicate the profiles at 250ms and inverted triangles and dotted curve indicate the profiles at 270ms, which are after the current ramp-up.

Fig.17 Time evolution of the neoclassical correction factor in the electrical conductivity and effective collisionality.  
The shaded area indicates the area where the Zeeman polarimeter is not applicable.

Fig.18 Comparison of calculated and measured current density profiles on the current ramp-up and the current ramp-down, where symbols are the measured profile from Zeeman polarimeter(ZP) and curves are the calculated profile by solving the magnetic diffusion equation.

The circles and solid curves indicate the current density profiles at 220ms before the current ramp-up and the current ramp-down, where they are started at 233ms. The squares and large broken curves indicate the profiles at 240ms which corresponds to during the current ramp-up and the current ramp-down. The diamonds and middle broken curves indicate the profiles at 260ms and the triangles and small broken curves indicate the profiles at 280ms, where both correspond to after the current ramp-up and the current ramp-down.

Fig.19 Time evolution of liner delta-prime ( $a\Delta'(0)$ ), saturated island width ( $w_s$ ) calculated by quasi-linear  $\Delta'$ -analysis, and calculated relative amplitude of poloidal-field fluctuations at plasma surface,  $[(\tilde{B}_\theta / B_\theta)_{r=a}]$ , where calculated results for  $m/n=2/1$ ,  $3/1$  and  $4/1$  are shown by solid squares, open circles and crosses, respectively. The island width  $w_s$  and  $(\tilde{B}_\theta / B_\theta)_{r=a}$  for  $m/n=2/1$  are not shown because they are too small ( $\approx 0$ ). The lowest figure also shows time evolutions of the safety factor at the plasma surface and magnetic fluctuations amplitude estimated from filtered magnetic probe signal, where solid and broken curves correspond to the signals in the frequency range of  $2 \leq f \leq 6$  kHz and  $5 \leq f \leq 12$  kHz, respectively.

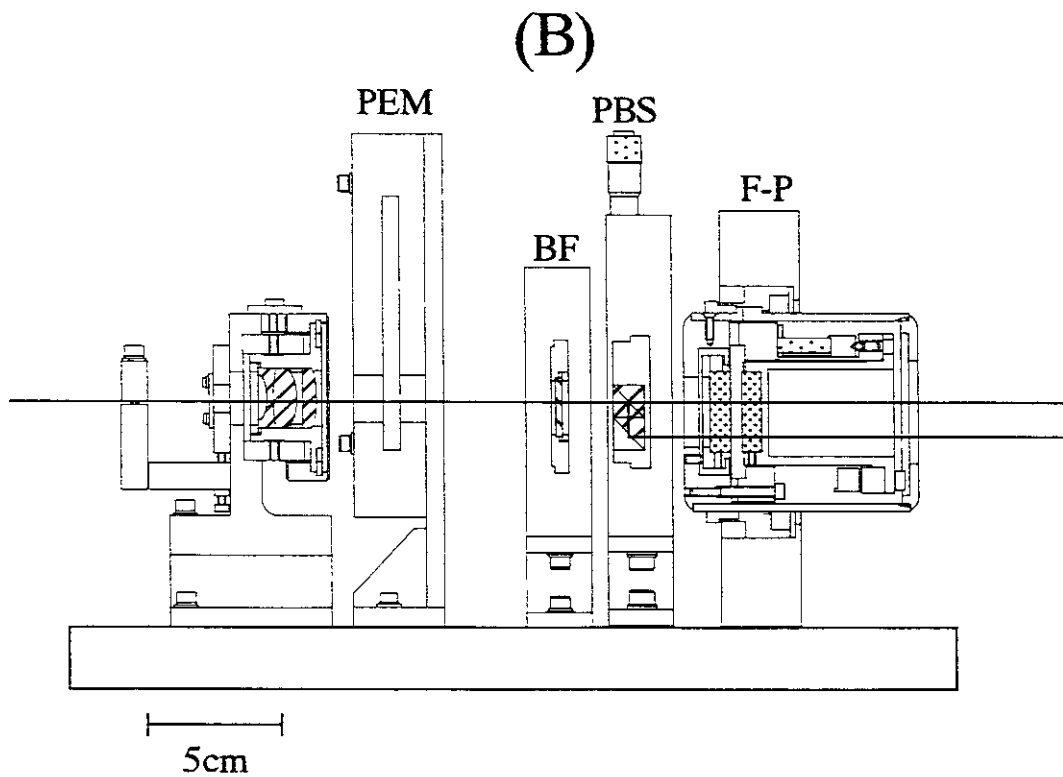
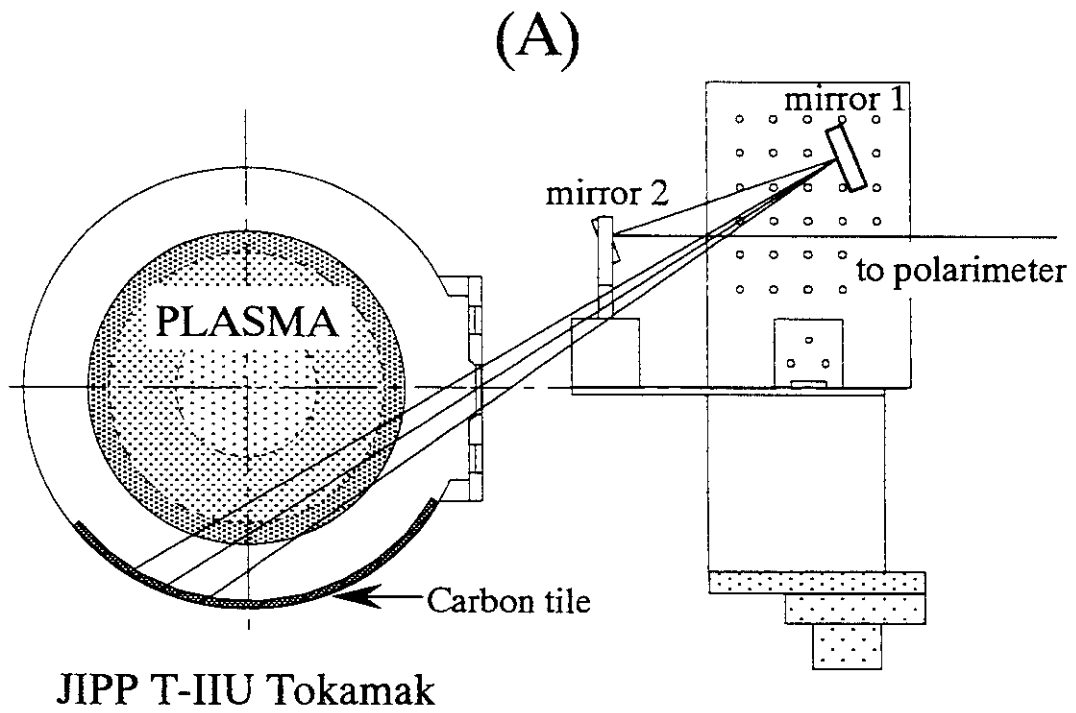


Figure 1



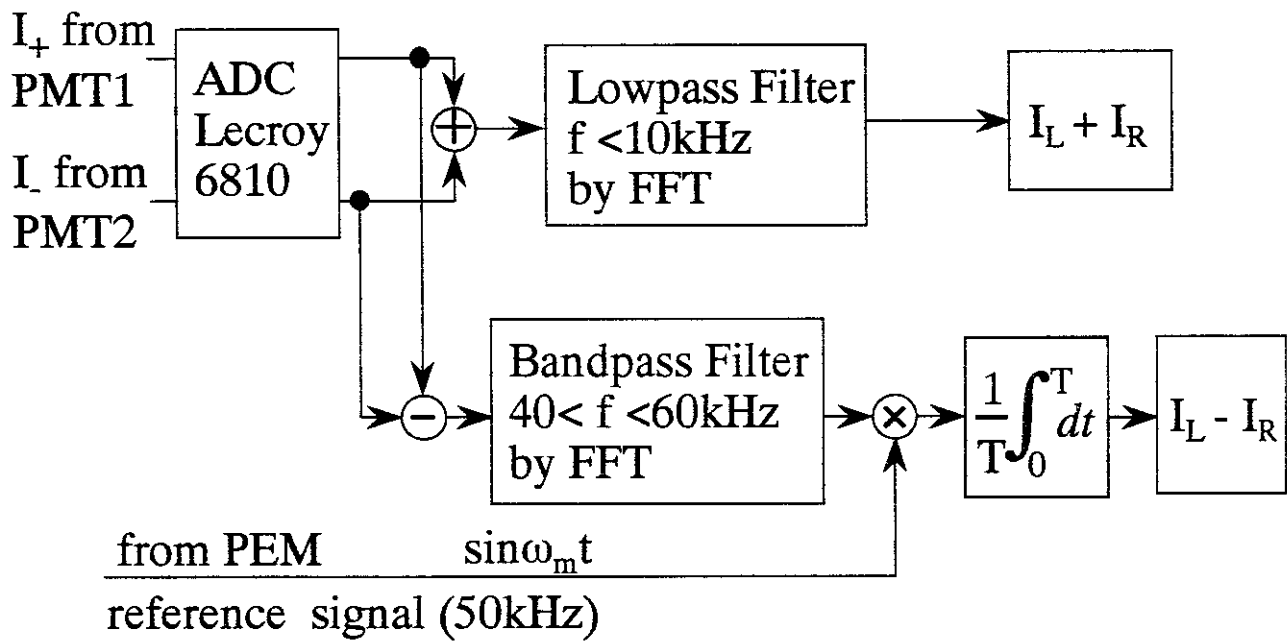


Figure 2

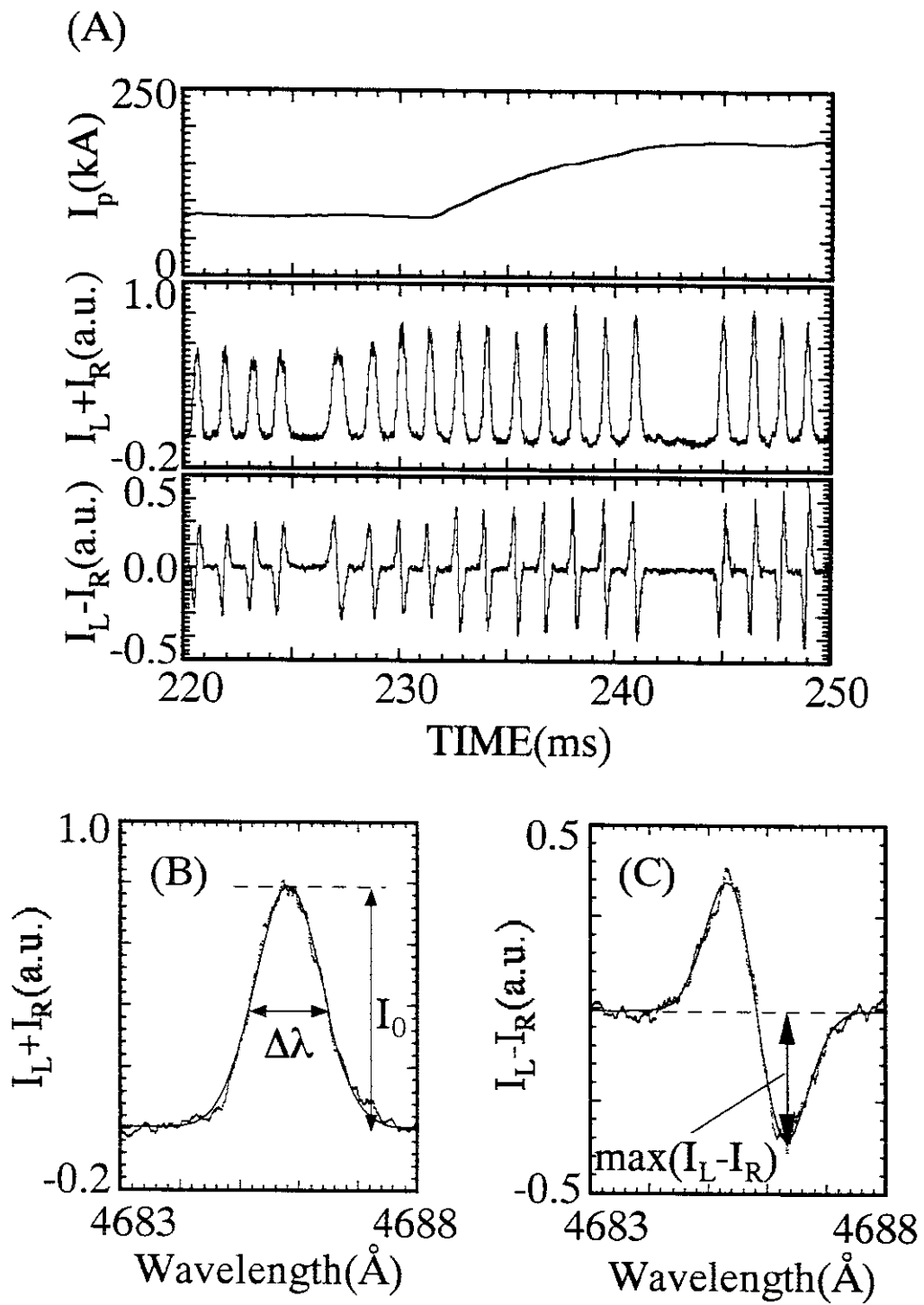


Figure 3

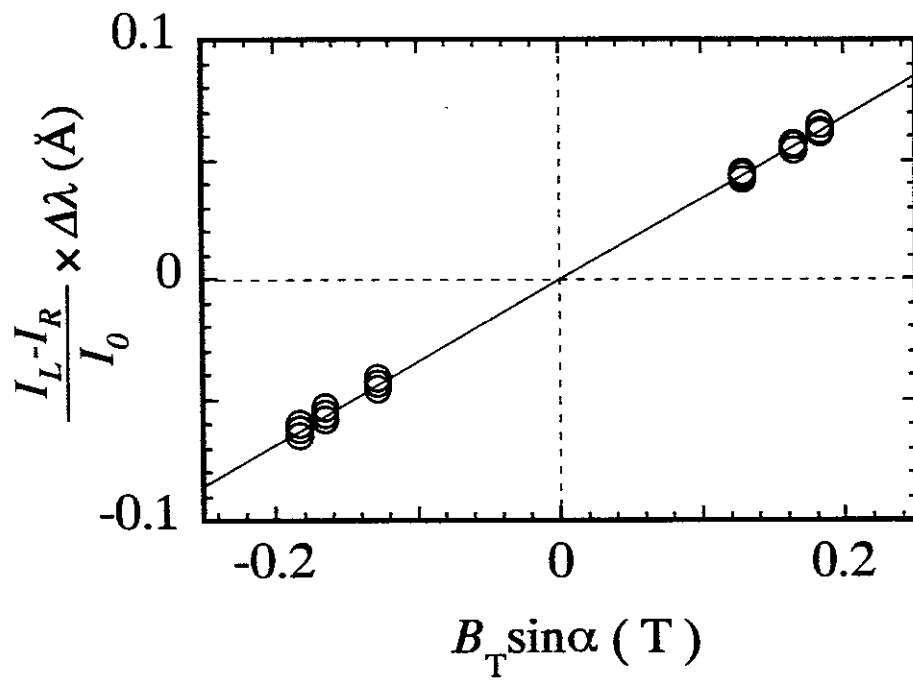


Figure 4

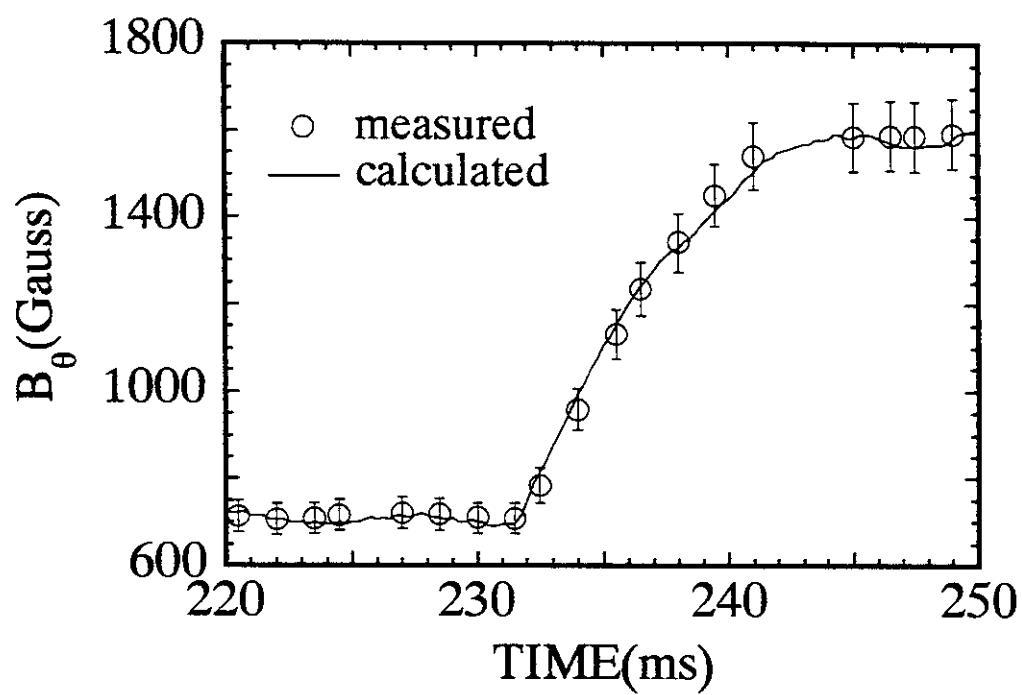


Figure 5

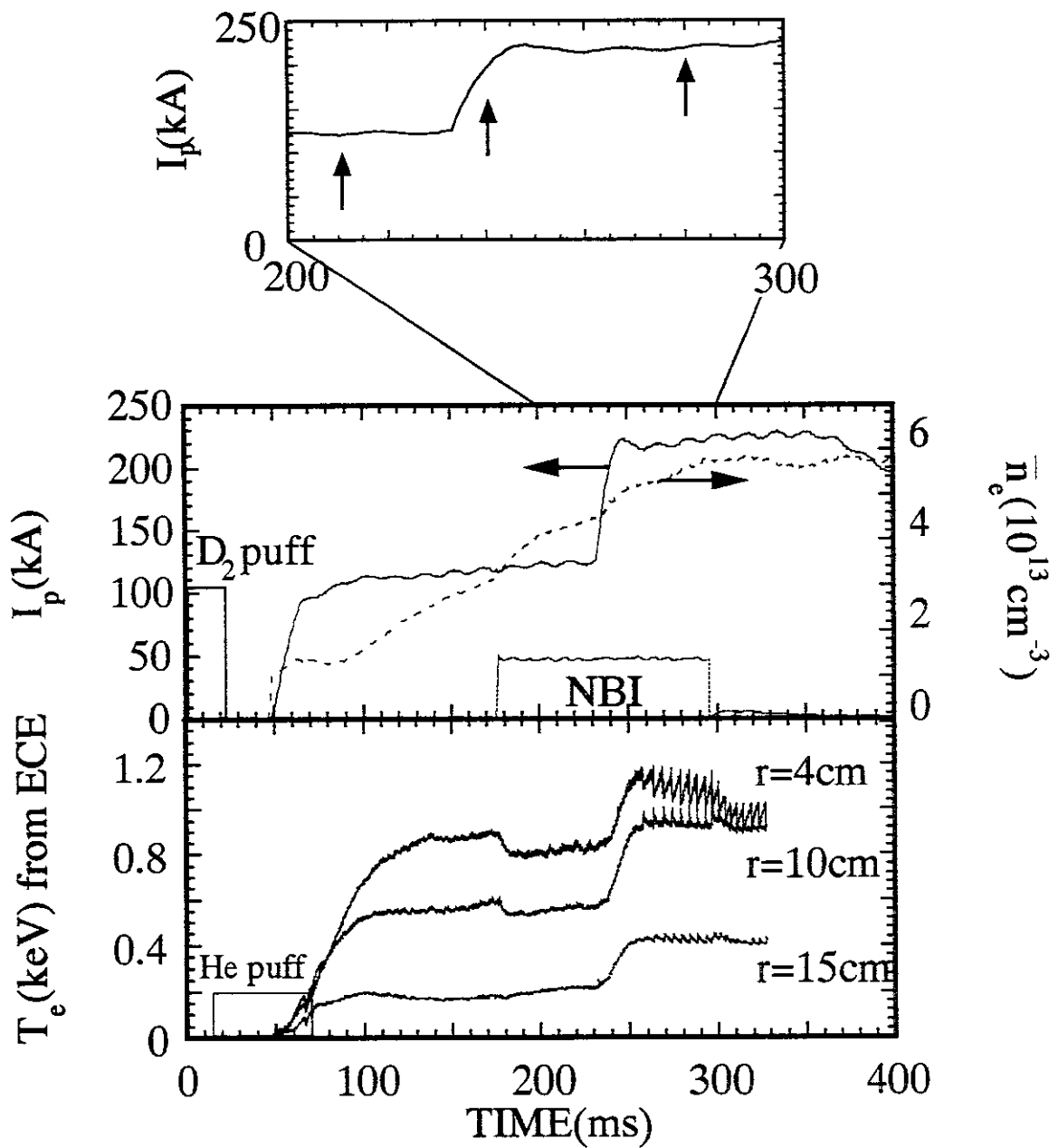


Figure 6

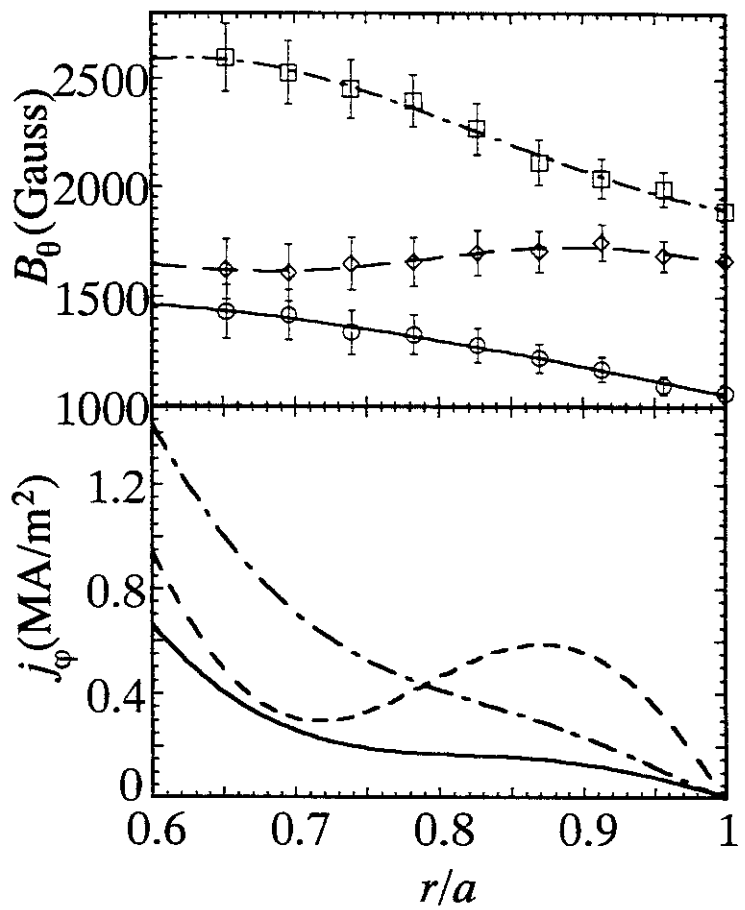


Figure 7

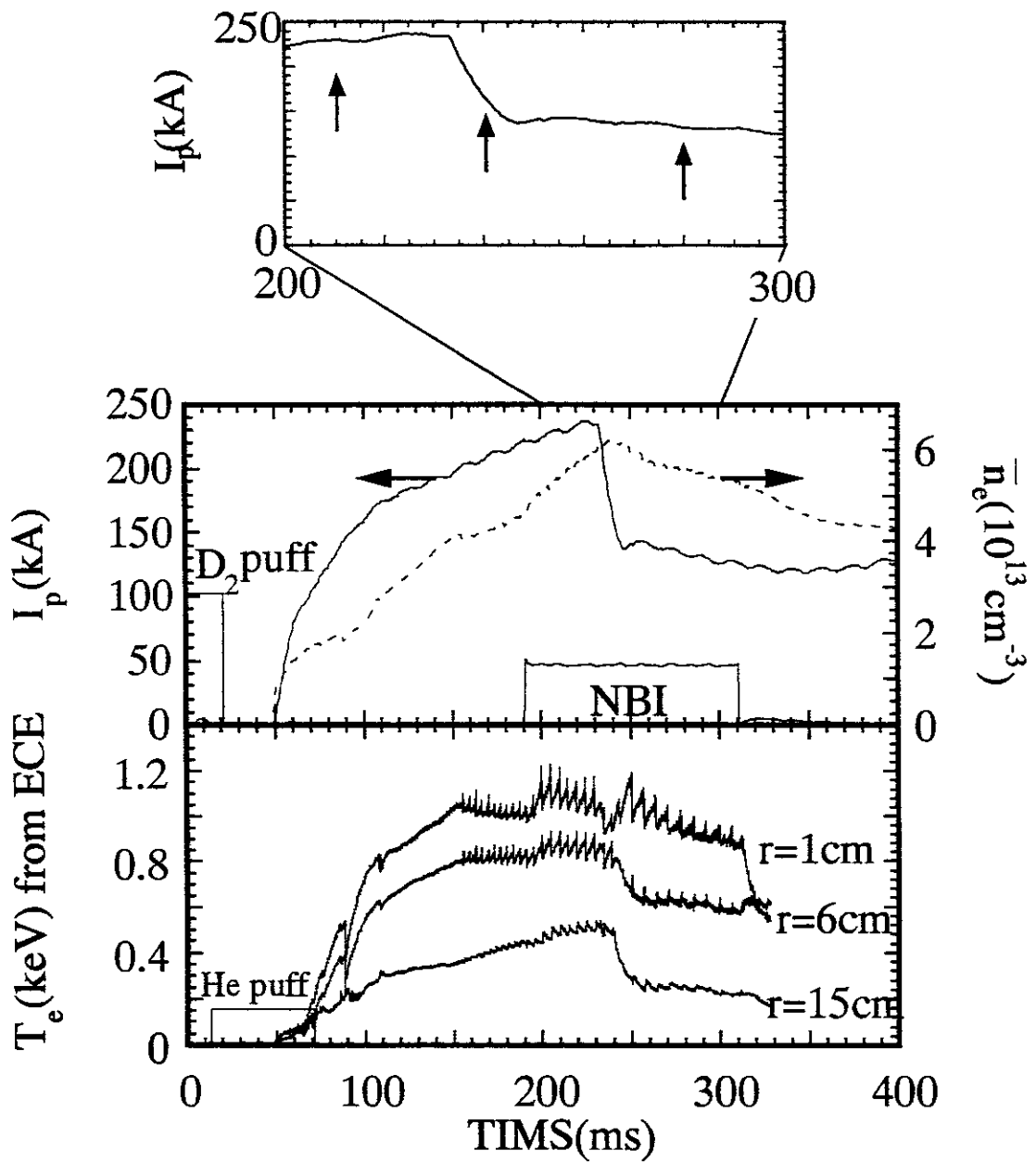


Figure 8

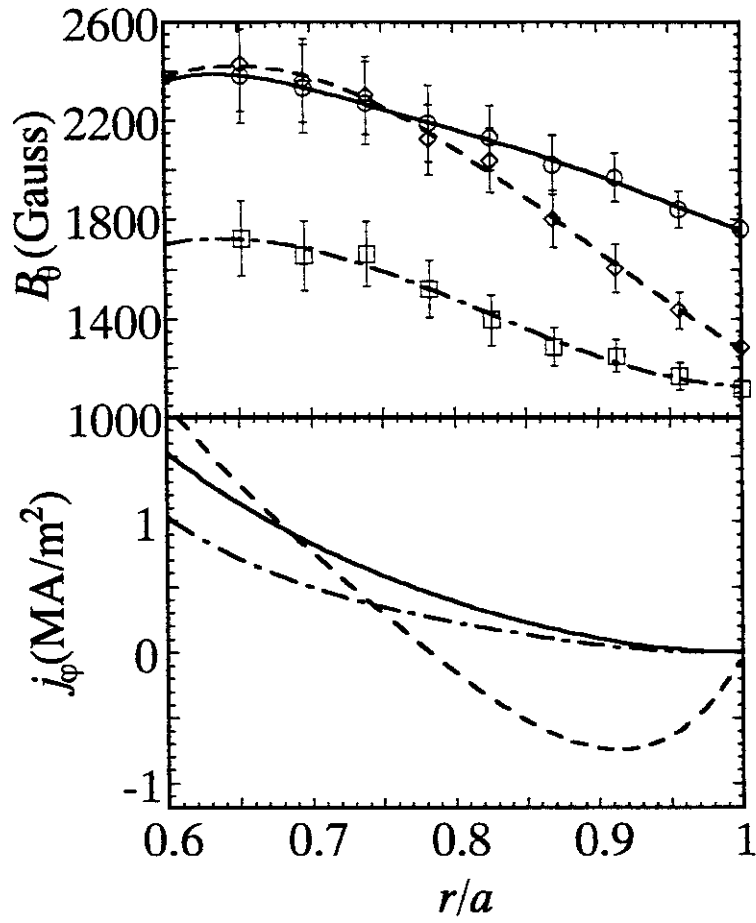


Figure 9



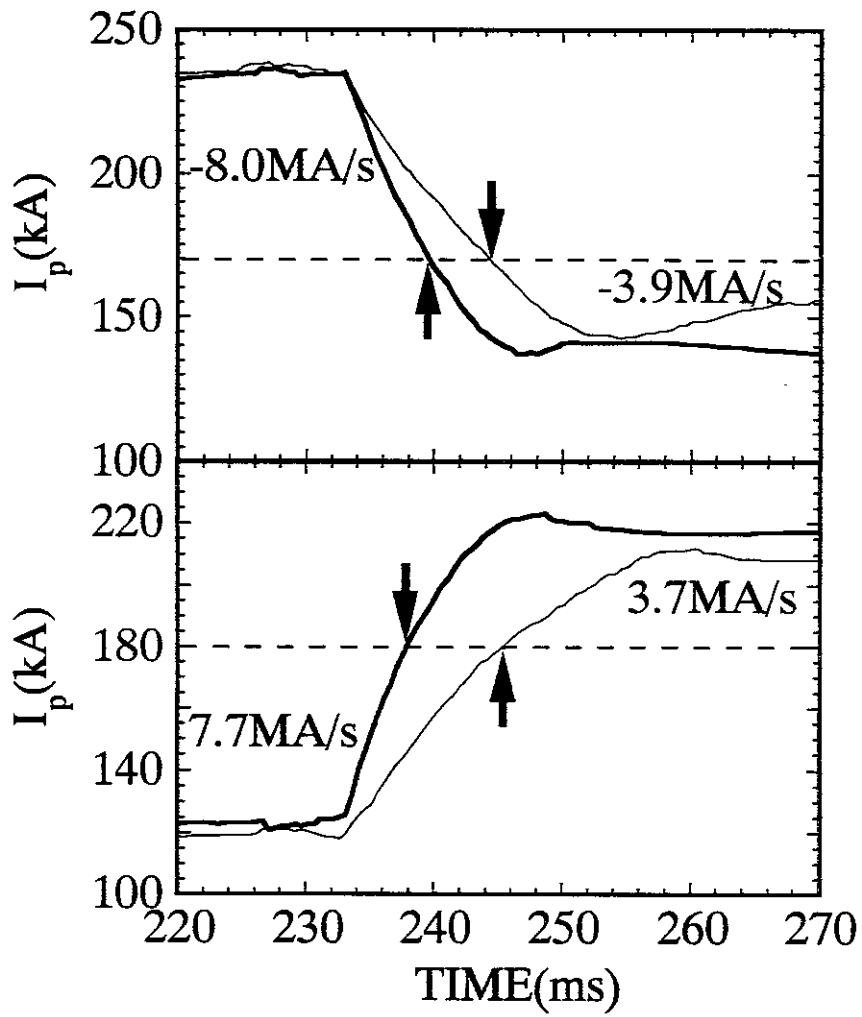


Figure 10

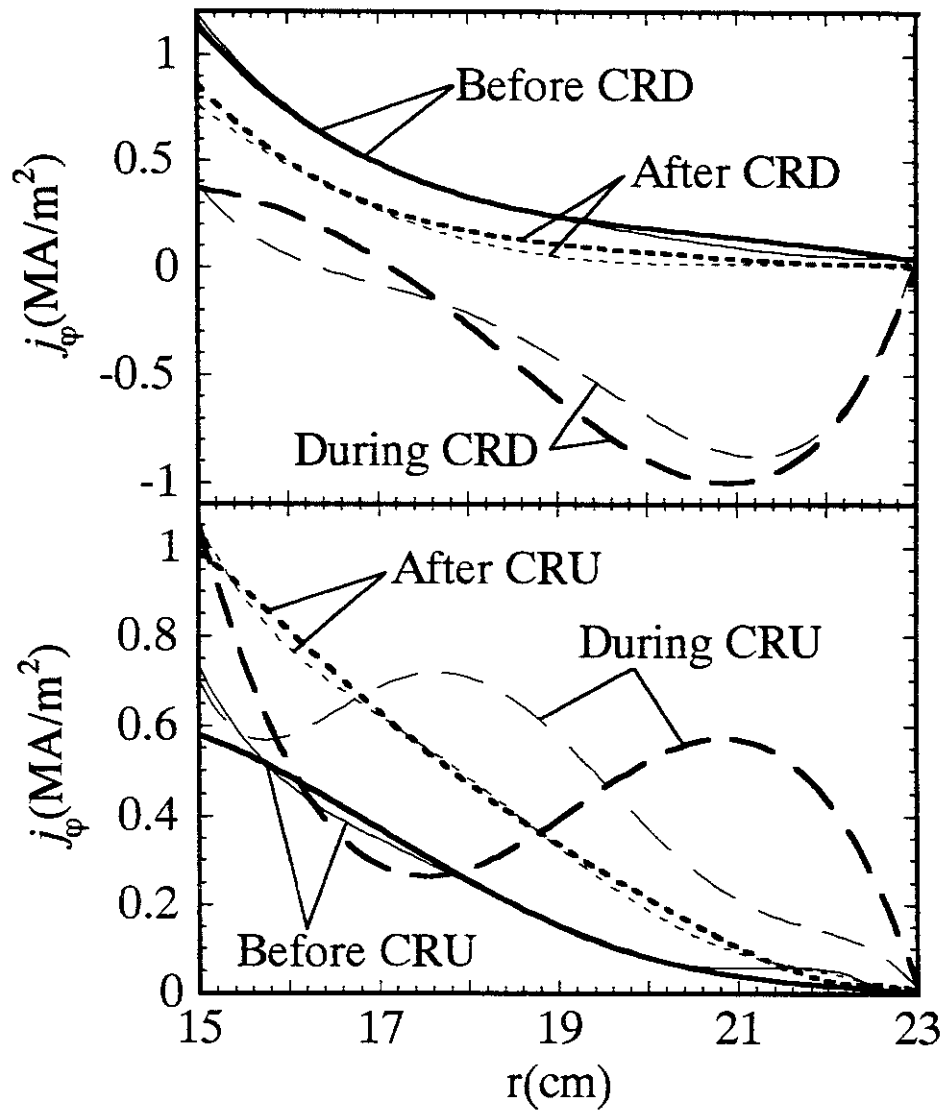


Figure 11

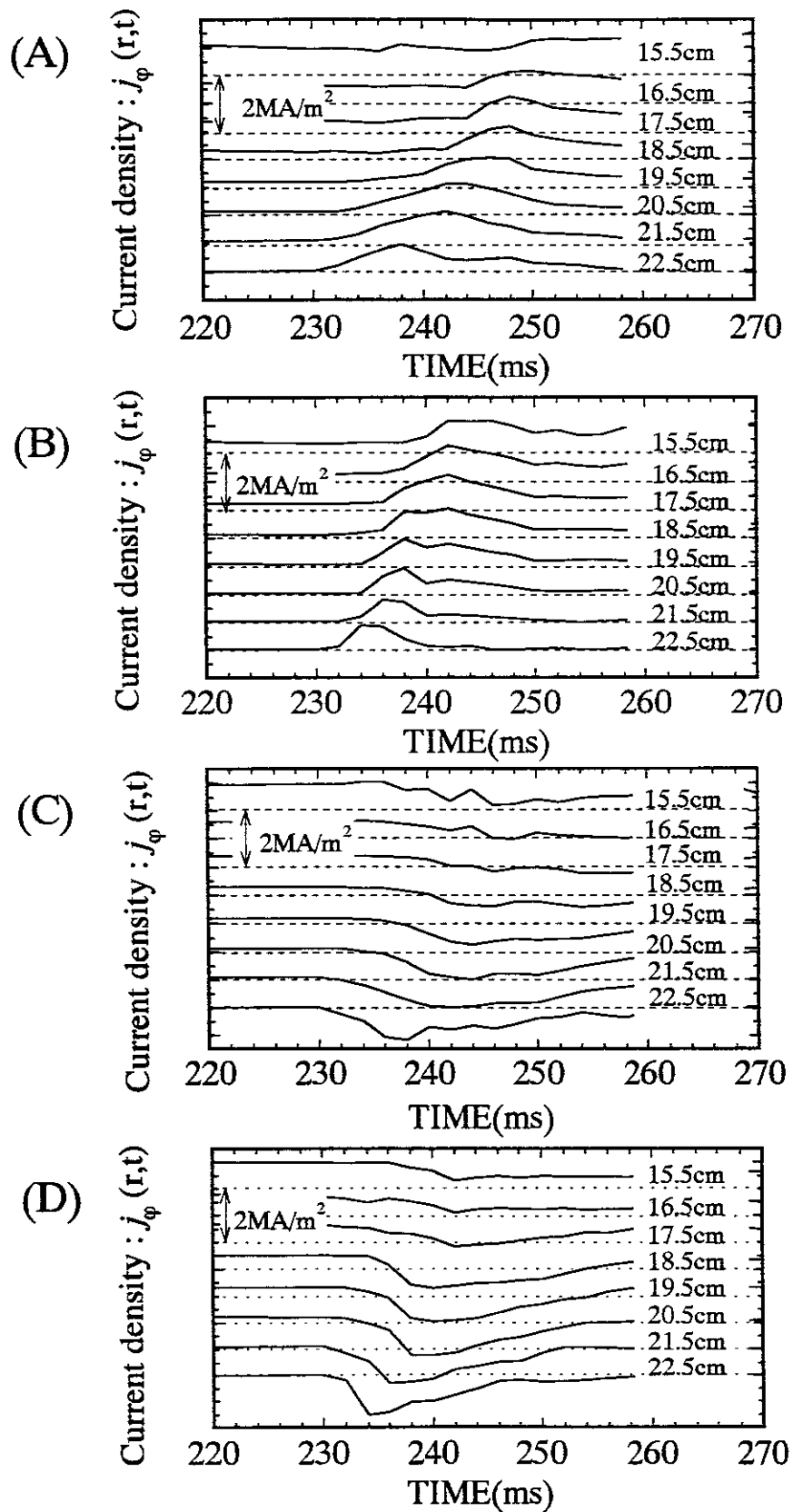


Figure 12

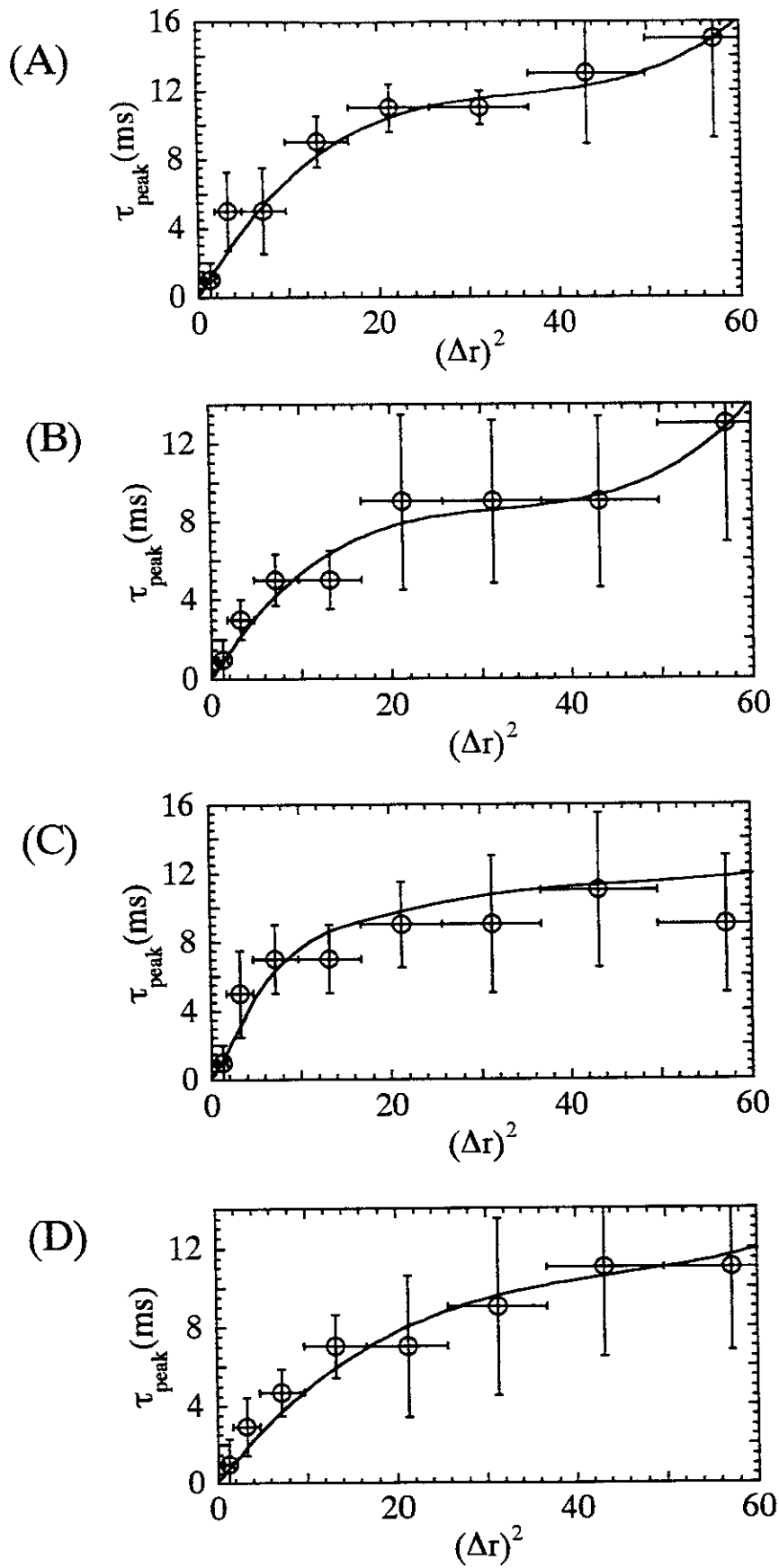


Figure 13

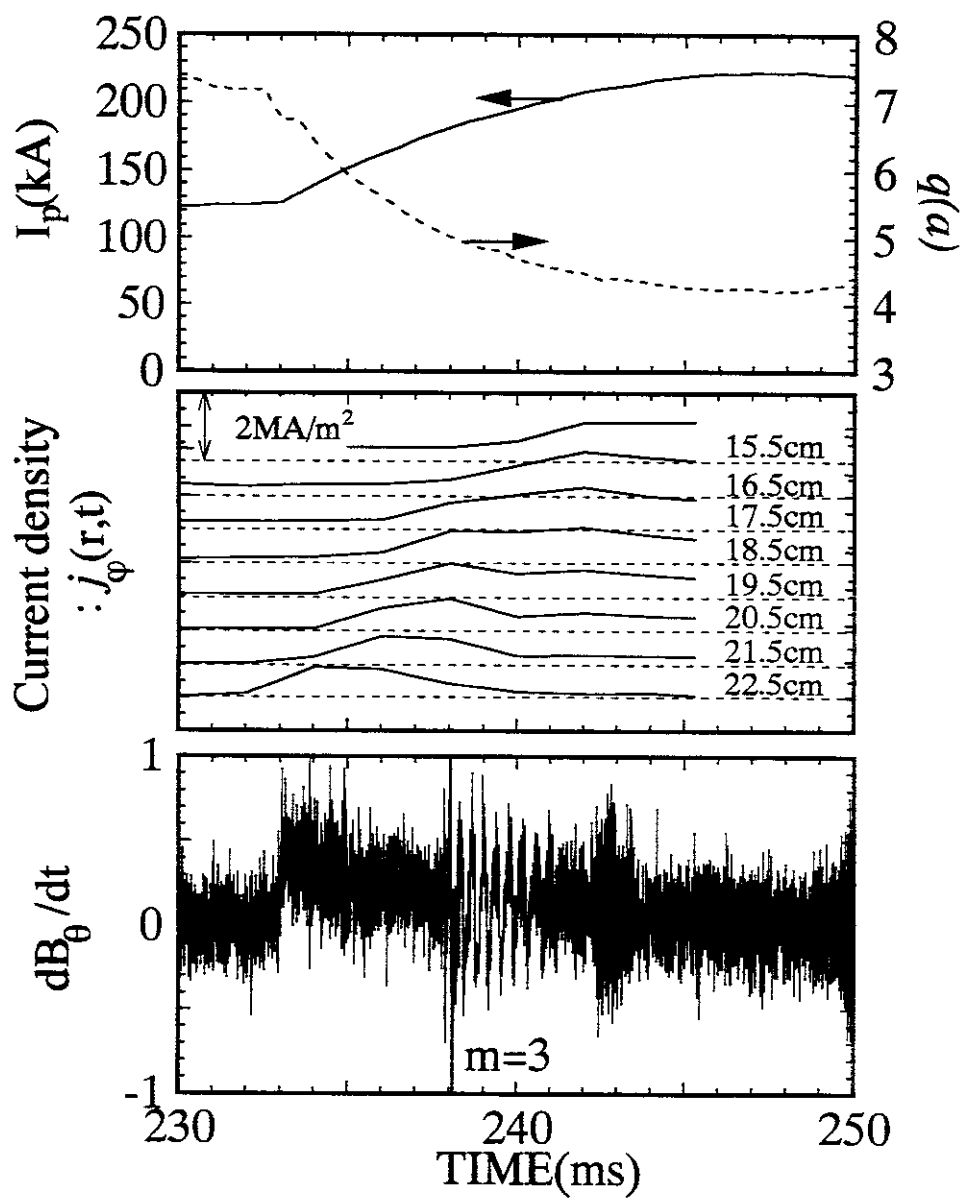


Figure 14

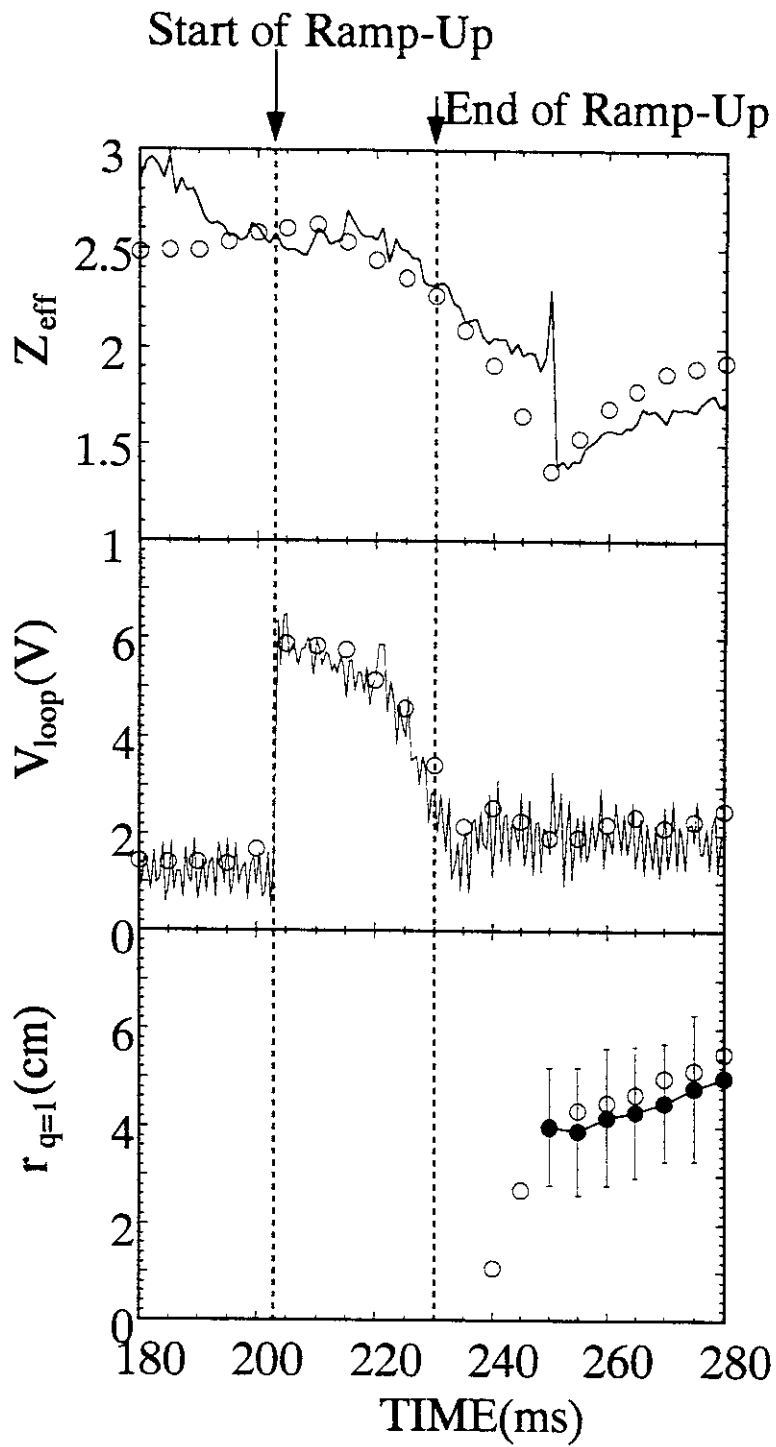


Figure 15

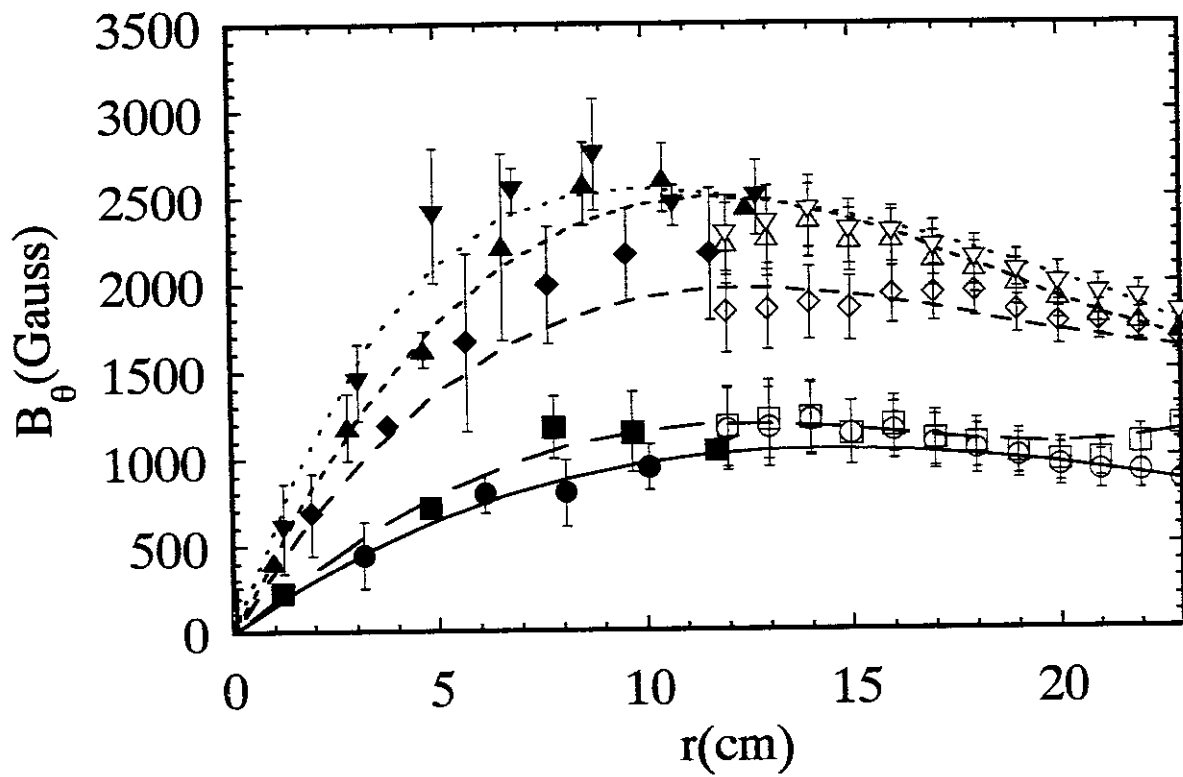


Figure 16

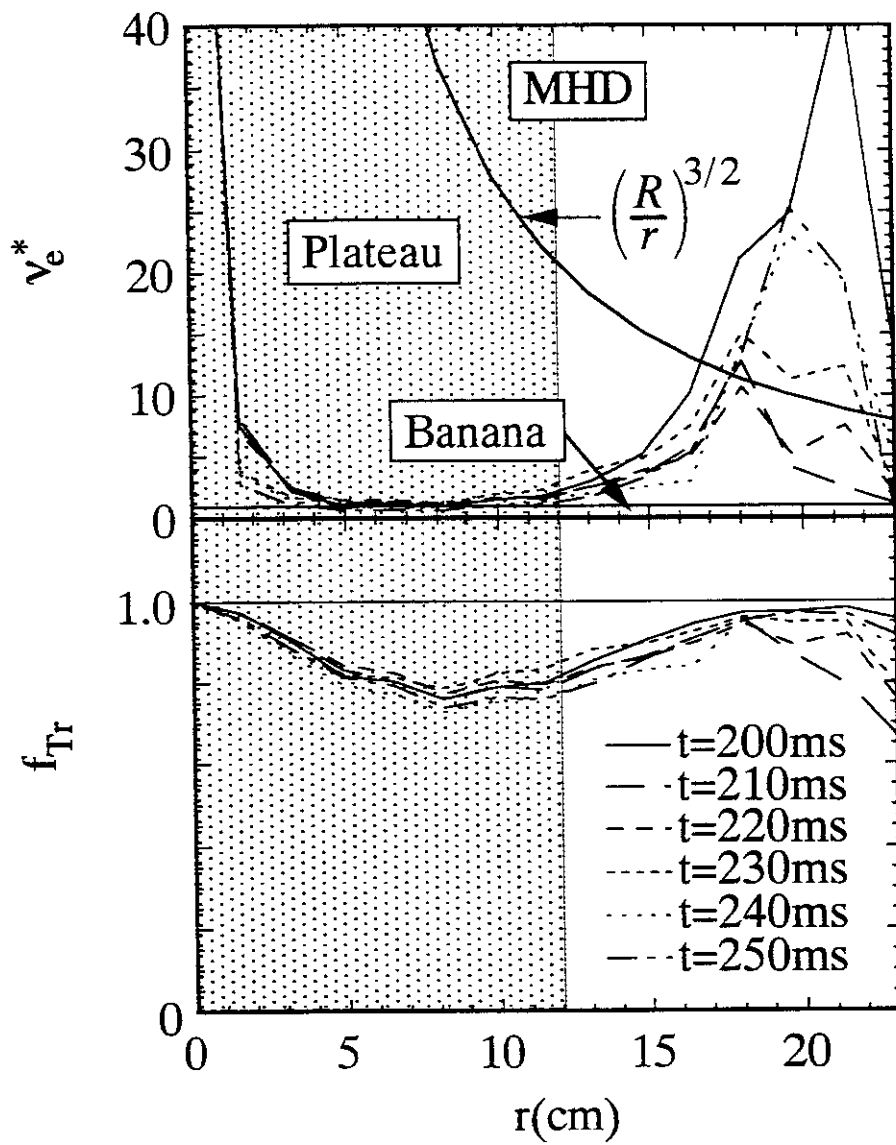


Figure 17



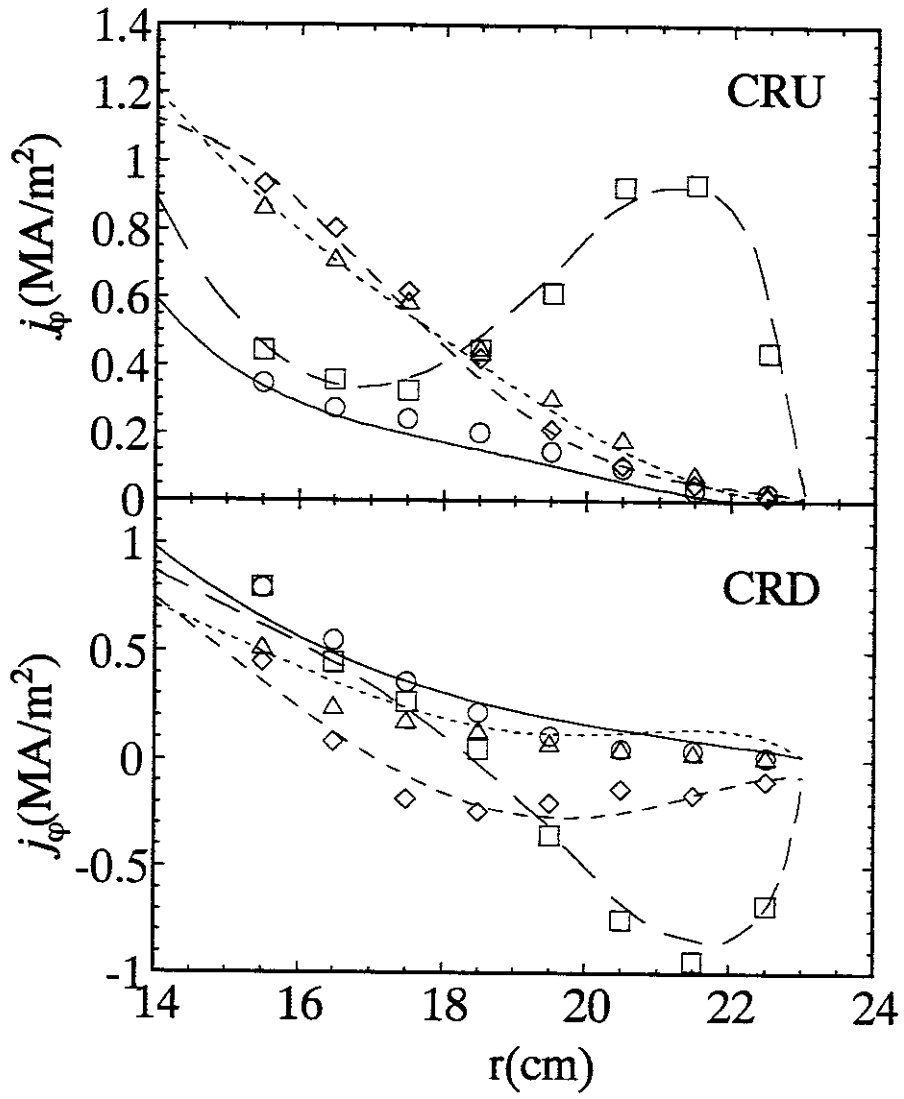


Figure 18

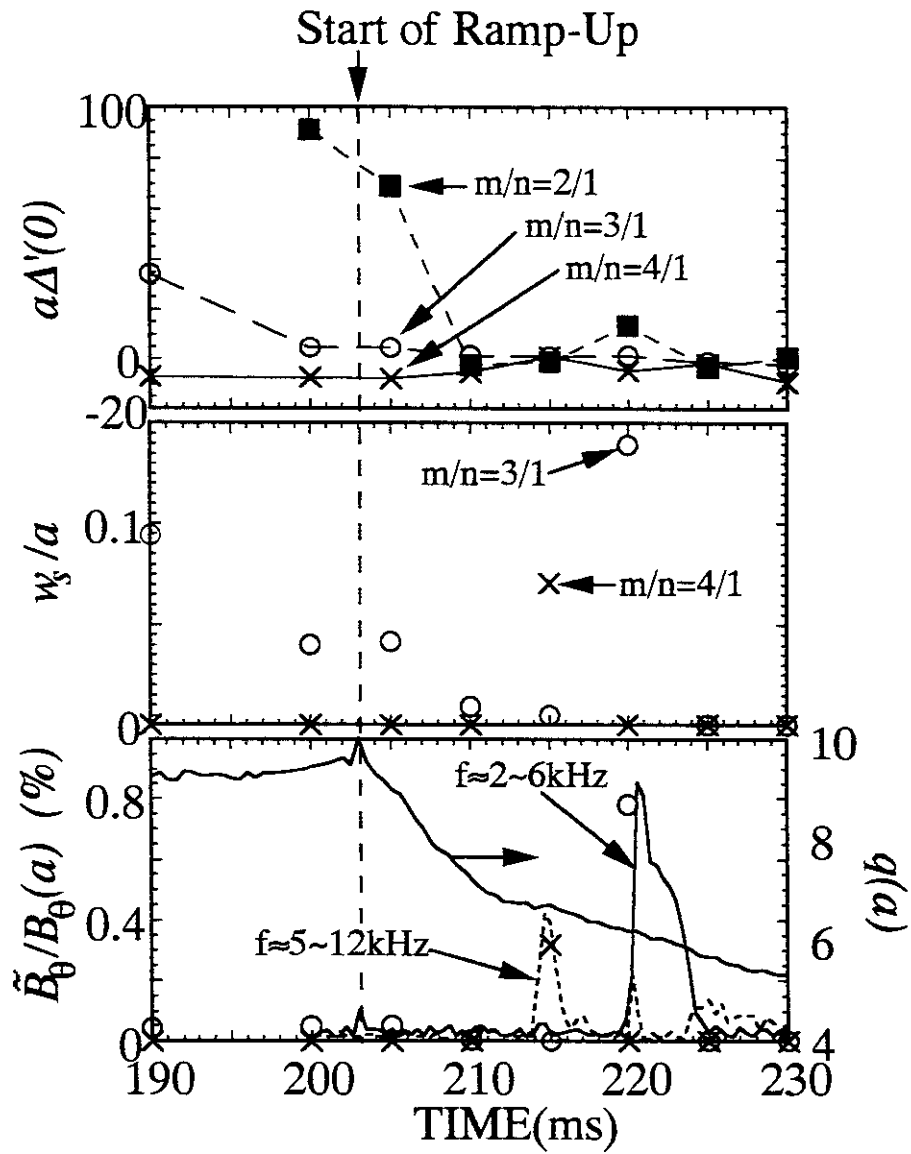


Figure 19

Table.I Specifications of the Zeeman polarimeter

	specifications
Fabry-Perot interferometer	
Free Spectral Range	5.4Å
Reflectivity	94%
Finess	50
Wavelength resolution	0.1Å
Flatness	$\lambda/100$
Aperture Diameter	22mm
PhotoElastic Modulator	
Optical Element Meterial	Fused Silica
Resonant Frequency	50kHz
Wavelength Transmittance Range	1800-26000Å
Aperture Diameter	16mm
Bandpass Filter	
Band Width	11Å(FWHM)
Aperture Diameter	20mm
Polarizing Beam Splitter	
Wavelength Transmittance Range	3900-5000Å
Transmissivity	>98%(for p polarized waves) < 2%(for s polarized waves)
Reflectivity	>98%(for s polarized waves) < 2%(for p polarized waves)

## Recent Issues of NIFS Series

- NIFS-438 A. Komori, N. Ohyabu, S. Masuzaki, T. Morisaki, H. Suzuki, C. Takahashi, S. Sakakibara, K. Watanabe, T. Watanabe, T. Minami, S. Morita, K. Tanaka, S. Ohdachi, S. Kubo, N. Inoue, H. Yamada, K. Nishimura, S. Okamura, K. Matsuoka, O. Motojima, M. Fujiwara, A. Iiyoshi, C. C. Klepper, J.F. Lyon, A.C. England, D.E. Greenwood, D.K. Lee, D.R. Overbey, J.A. Rome, D.E. Schechter and C.T. Wilson,  
*Edge Plasma Control by a Local Island Divertor in the Compact Helical System; Sep. 1996 (IAEA-CN-64/C1-2)*
- NIFS-439 K. Ida, K. Kondo, K. Nagasaki, T. Hamada, H. Zushi, S. Hidekuma, F. Sano, T. Mizuuchi, H. Okada, S. Besshou, H. Funaba, Y. Kurimoto, K. Watanabe and T. Obiki,  
*Dynamics of Ion Temperature in Heliotron-E; Sep. 1996 (IAEA-CN-64/CP-5)*
- NIFS-440 S. Morita, H. Idei, H. Iguchi, S. Kubo, K. Matsuoka, T. Minami, S. Okamura, T. Ozaki, K. Tanaka, K. Toi, R. Akiyama, A. Ejiri, A. Fujisawa, M. Fujiwara, M. Goto, K. Ida, N. Inoue, A. Komori, R. Kumazawa, S. Masuzaki, T. Morisaki, S. Muto, K. Narihara, K. Nishimura, I. Nomura, S. Ohdachi, M. Osakabe, A. Sagara, Y. Shirai, H. Suzuki, C. Takahashi, K. Tsumori, T. Watari, H. Yamada and I. Yamada,  
*A Study on Density Profile and Density Limit of NBI Plasmas in CHS; Sep. 1996 (IAEA-CN-64/CP-3)*
- NIFS-441 O. Kaneko, Y. Takeiri, K. Tsumori, Y. Oka, M. Osakabe, R. Akiyama, T. Kawamoto, E. Asano and T. Kuroda,  
*Development of Negative-Ion-Based Neutral Beam Injector for the Large Helical Device; Sep. 1996 (IAEA-CN-64/GP-9)*
- NIFS-442 K. Toi, K.N. Sato, Y. Hamada, S. Ohdachi, H. Sakakita, A. Nishizawa, A. Ejiri, K. Narihara, H. Kuramoto, Y. Kawasumi, S. Kubo, T. Seki, K. Kitachi, J. Xu, K. Ida, K. Kawahata, I. Nomura, K. Adachi, R. Akiyama, A. Fujisawa, J. Fujita, N. Hiraki, S. Hidekuma, S. Hirokura, H. Idei, T. Ido, H. Iguchi, K. Iwasaki, M. Isobe, O. Kaneko, Y. Kano, M. Kojima, J. Koog, R. Kumazawa, T. Kuroda, J. Li, R. Liang, T. Minami, S. Morita, K. Ohkubo, Y. Oka, S. Okajima, M. Osakabe, Y. Sakawa, M. Sasao, K. Sato, T. Shimpo, T. Shoji, H. Sugai, T. Watari, I. Yamada and K. Yamauti,  
*Studies of Perturbative Plasma Transport, Ice Pellet Ablation and Sawtooth Phenomena in the JIPP T-IIU Tokamak; Sep. 1996 (IAEA-CN-64/A6-5)*
- NIFS-443 Y. Todo, T. Sato and The Complexity Simulation Group,  
*Vlasov-MHD and Particle-MHD Simulations of the Toroidal Alfvén Eigenmode; Sep. 1996 (IAEA-CN-64/D2-3)*
- NIFS-444 A. Fujisawa, S. Kubo, H. Iguchi, H. Idei, T. Minami, H. Sanuki, K. Itoh, S. Okamura, K. Matsuoka, K. Tanaka, S. Lee, M. Kojima, T.P. Crowley, Y. Hamada, M. Iwase, H. Nagasaki, H. Suzuki, N. Inoue, R. Akiyama, M. Osakabe, S. Morita, C. Takahashi, S. Muto, A. Ejiri, K. Ida, S. Nishimura, K. Narihara, I. Yamada,

- K. Toi, S. Ohdachi, T. Ozaki, A. Komori, K. Nishimura, S. Hidekuma, K. Ohkubo, D.A. Rasmussen, J.B. Wilgen, M. Murakami, T. Watari and M. Fujiwara, *An Experimental Study of Plasma Confinement and Heating Efficiency through the Potential Profile Measurements with a Heavy Ion Beam Probe in the Compact Helical System*; Sep. 1996 (IAEA-CN-64/C1-5)
- NIFS-445 O. Motojima, N. Yanagi, S. Imagawa, K. Takahata, S. Yamada, A. Iwamoto, H. Chikaraishi, S. Kitagawa, R. Maekawa, S. Masuzaki, T. Mito, T. Morisaki, A. Nishimura, S. Sakakibara, S. Satoh, T. Satow, H. Tamura, S. Tanahashi, K. Watanabe, S. Yamaguchi, J. Yamamoto, M. Fujiwara and A. Iiyoshi, *Superconducting Magnet Design and Construction of LHD*; Sep. 1996 (IAEA-CN-64/G2-4)
- NIFS-446 S. Murakami, N. Nakajima, S. Okamura, M. Okamoto and U. Gasparino, *Orbit Effects of Energetic Particles on the Reachable  $\beta$ -Value and the Radial Electric Field in NBI and ECR Heated Heliotron Plasmas*; Sep. 1996 (IAEA-CN-64/CP -6) Sep. 1996
- NIFS-447 K. Yamazaki, A. Sagara, O. Motojima, M. Fujiwara, T. Amano, H. Chikaraishi, S. Imagawa, T. Muroga, N. Noda, N. Ohyabu, T. Satow, J.F. Wang, K.Y. Watanabe, J. Yamamoto, H. Yamanishi, A. Kohyama, H. Matsui, O. Mitarai, T. Noda, A.A. Shishkin, S. Tanaka and T. Terai *Design Assessment of Heliotron Reactor*; Sep. 1996 (IAEA-CN-64/G1-5)
- NIFS-448 M. Ozaki, T. Sato and the Complexity Simulation Group, *Interactions of Convecting Magnetic Loops and Arcades*; Sep. 1996
- NIFS-449 T. Aoki, *Interpolated Differential Operator (IDO) Scheme for Solving Partial Differential Equations*; Sep. 1996
- NIFS-450 D. Biskamp and T. Sato, *Partial Reconnection in the Sawtooth Collapse*; Sep. 1996
- NIFS-451 J. Li, X. Gong, L. Luo, F.X. Yin, N. Noda, B. Wan, W. Xu, X. Gao, F. Yin, J.G. Jiang, Z. Wu., J.Y. Zhao, M. Wu, S. Liu and Y. Han, *Effects of High Z Probe on Plasma Behavior in HT-6M Tokamak*; Sep. 1996
- NIFS-452 N. Nakajima, K. Ichiguchi, M. Okamoto and R.L. Dewar, *Ballooning Modes in Heliotrons/Torsatrons*; Sep. 1996 (IAEA-CN-64/D3-6)
- NIFS-453 A. Iiyoshi, *Overview of Helical Systems*; Sep. 1996 (IAEA-CN-64/O1-7)
- NIFS-454 S. Saito, Y. Nomura, K. Hirose and Y.H. Ichikawa, *Separatrix Reconnection and Periodic Orbit Annihilation in the Harper Map*; Oct. 1996
- NIFS-455 K. Ichiguchi, N. Nakajima and M. Okamoto,

*Topics on MHD Equilibrium and Stability in Heliotron / Torsatron*; Oct. 1996

- NIFS-456 G. Kawahara, S. Kida, M. Tanaka and S. Yanase,  
*Wrap, Tilt and Stretch of Vorticity Lines around a Strong Straight Vortex Tube in a Simple Shear Flow*; Oct. 1996
- NIFS-457 K. Itoh, S.-I. Itoh, A. Fukuyama and M. Yagi,  
*Turbulent Transport and Structural Transition in Confined Plasmas*; Oct. 1996
- NIFS-458 A. Kageyama and T. Sato,  
*Generation Mechanism of a Dipole Field by a Magnetohydrodynamic Dynamo*; Oct. 1996
- NIFS-459 K. Araki, J. Mizushima and S. Yanase,  
*The Non-axisymmetric Instability of the Wide-Gap Spherical Couette Flow*; Oct. 1996
- NIFS-460 Y. Hamada, A. Fujisawa, H. Iguchi, A. Nishizawa and Y. Kawasumi,  
*A Tandem Parallel Plate Analyzer*; Nov. 1996
- NIFS-461 Y. Hamada, A. Nishizawa, Y. Kawasumi, A. Fujisawa, K. Narihara, K. Ida, A. Ejiri, S. Ohdachi, K. Kawahata, K. Toi, K. Sato, T. Seki, H. Iguchi, K. Adachi, S. Hidekuma, S. Hirokura, K. Iwasaki, T. Ido, M. Kojima, J. Koong, R. Kumazawa, H. Kuramoto, T. Minami, I. Nomura, H. Sakakita, M. Sasao, K.N. Sato, T. Tsuzuki, J. Xu, I. Yamada and T. Watari,  
*Density Fluctuation in JIPP T-IIU Tokamak Plasmas Measured by a Heavy Ion Beam Probe*; Nov. 1996
- NIFS-462 N. Katsuragawa, H. Hojo and A. Mase,  
*Simulation Study on Cross Polarization Scattering of Ultrashort-Pulse Electromagnetic Waves*; Nov. 1996
- NIFS-463 V. Voitsenya, V. Konovalov, O. Motojima, K. Narihara, M. Becker and B. Schunke,  
*Evaluations of Different Metals for Manufacturing Mirrors of Thomson Scattering System for the LHD Divertor Plasma*; Nov. 1996
- NIFS-464 M. Pereyaslavets, M. Sato, T. Shimojima, Y. Takita, H. Idei, S. Kubo, K. Ohkubo and K. Hayashi,  
*Development and Simulation of RF Components for High Power Millimeter Wave Gyrotrons*; Nov. 1997
- NIFS-465 V.S. Voitsenya, S. Masuzaki, O. Motojima, N. Noda and N. Ohyabu,  
*On the Use of CX Atom Analyzer for Study Characteristics of Ion Component in a LHD Divertor Plasma*; Dec. 1996
- NIFS-466 H. Miura and S. Kida,  
*Identification of Tubular Vortices in Complex Flows*; Dec. 1996

- NIFS-467 Y. Takeiri, Y. Oka, M. Osakabe, K. Tsumori, O. Kaneko, T. Takanashi, E. Asano, T. Kawamoto, R. Akiyama and T. Kuroda,  
*Suppression of Accelerated Electrons in a High-current Large Negative Ion Source*; Dec. 1996
- NIFS-468 A. Sagara, Y. Hasegawa, K. Tsuzuki, N. Inoue, H. Suzuki, T. Morisaki, N. Noda, O. Motojima, S. Okamura, K. Matsuoka, R. Akiyama, K. Ida, H. Idei, K. Iwasaki, S. Kubo, T. Minami, S. Morita, K. Narihara, T. Ozaki, K. Sato, C. Takahashi, K. Tanaka, K. Toi and I. Yamada,  
*Real Time Boronization Experiments in CHS and Scaling for LHD*; Dec. 1996
- NIFS-469 V.L. Vdovin, T. Watari and A. Fukuyama,  
*3D Maxwell-Vlasov Boundary Value Problem Solution in Stellarator Geometry in Ion Cyclotron Frequency Range (final report)*; Dec. 1996
- NIFS-470 N. Nakajima, M. Yokoyama, M. Okamoto and J. Nührenberg,  
*Optimization of M=2 Stellarator*; Dec. 1996
- NIFS-471 A. Fujisawa, H. Iguchi, S. Lee and Y. Hamada,  
*Effects of Horizontal Injection Angle Displacements on Energy Measurements with Parallel Plate Energy Analyzer*; Dec. 1996
- NIFS-472 R. Kanno, N. Nakajima, H. Sugama, M. Okamoto and Y. Ogawa,  
*Effects of Finite- $\beta$  and Radial Electric Fields on Neoclassical Transport in the Large Helical Device*; Jan. 1997
- NIFS-473 S. Murakami, N. Nakajima, U. Gasparino and M. Okamoto,  
*Simulation Study of Radial Electric Field in CHS and LHD*; Jan. 1997
- NIFS-474 K. Ohkubo, S. Kubo, H. Idei, M. Sato, T. Shimozuma and Y. Takita,  
*Coupling of Tilting Gaussian Beam with Hybrid Mode in the Corrugated Waveguide*; Jan. 1997
- NIFS-475 A. Fujisawa, H. Iguchi, S. Lee and Y. Hamada,  
*Consideration of Fluctuation in Secondary Beam Intensity of Heavy Ion Beam Probe Measurements*; Jan. 1997
- NIFS-476 Y. Takeiri, M. Osakabe, Y. Oka, K. Tsumori, O. Kaneko, T. Takanashi, E. Asano, T. Kawamoto, R. Akiyama and T. Kuroda,  
*Long-pulse Operation of a Cesium-Seeded High-Current Large Negative Ion Source*; Jan. 1997
- NIFS-477 H. Kuramoto, K. Toi, N. Haraki, K. Sato, J. Xu, A. Ejiri, K. Narihara, T. Seki, S. Ohdachi, K. Adati, R. Akiyama, Y. Hamada, S. Hirokura, K. Kawahata and M. Kojima,  
*Study of Toroidal Current Penetration during Current Ramp in JIPP T-IIU with Fast Response Zeeman Polarimeter*; Jan. 7, 1997